Laplacian growth patterns

A study of boundary evolution using iterated conformal maps and Loewner evolution

Bodil Oust

Thesis submitted for the degree
Master of Science

Physics of Geological Processes
Department of Physics
University of Oslo
Norway

May 2009

Norwegian Centre of Excellence
PGP PHYSICS OF GEOLOGICAL PROCESSES
UNIVERSITY OF OSLO

Acknowledgements

I would like to acknowledge my supervisor, Joachim Mathiesen, for guiding me through this project. The outcome of this study would never have been the same without a Dane to keep me on the track and telling me to work harder whenever I was beeing unproductive. I am fascinated by the great patience that you posess, Joachim.

Whenever Joachim was not there, I would direct most of my questions to Espen Jettestuen. And Espen would always answer, whether it beeing a question about the inner secrets of mathematics or some Matlab syntax.

I have learnt that contacts are important. When writing a thesis in a foreign language, it is always good to have a native speaker of that language to remove all funny expressions and misspellings. Thank you so much Kirsten!

I have never before experienced having only one class mate, but I am pretty sure that nobody else could have fulfilled that task better than how Magnus has done. Kristin has made me several liters of coffee, which certainly has been essential for keeping me going. Thanks to both of you for distracting me with discussions and small talk whenever I obviously needed a break.

All the people at PGP deserve to be mentioned, just because all of you are important contributors to an inspiring and social working environment. A special thanks to those that were there and sang both verses of "Hurra for deg" to me on my 25th birthday. I really appreciated that.

Abstract

Many of the patterns that can be observed in nature or in experiments are the result of surface instabilities. These structures typically arise when an interface is forced to move due to fluxes of heat and/or mass or because of a mechanical forcing that leads to a pressure gradient. A small perturbation of the moving boundary will either grow unstably or decay such that the boundary recovers its original shape. The stability of such a perturbation is determined by the geometry of the surface together with the thermodynamic and material properties relevant to the specific problem. If the conditions are such that the moving boundary is unstable, it will evolve into some kind of a pattern. The characteristics and morphology of the final structure will also depend on the parameters that determine the stability of the interface.

If the temperature, concentration or pressure field that controls the process satisfy the Laplace equation, it belongs to an important category of surface evolution processes called Laplacian growth problems. In such problems, the interface velocity is a function of the gradient of the Laplacian field. Laplacian growth is viewed as a fundamental model for pattern formation [Bazant and Crowdy, 2005]. Both radial and directional growth are considered in this thesis.

Laplacian growth problems can be solved by means of conformal mapping techniques. Viscous fingering, electrochemical deposition and the growth of bacterial colonies are examples of Laplacian growth processes that often occur in radial geometry. There are many different approaches to the study of these patterns, both discrete and continuous. In order to obtain a conformally invariant boundary condition in the model,

surface tension must be zero or constant. If no other regularisation is introduced, this will lead to the formation of singularities on the boundary in finite time.

The techniques used in radial geometry involve analytic solutions that are harder to handle for directional growth. The Loewner differential equation for conformal maps is therefore used to study these problems. Examples of relevant processes are fluidisation experiments, channel formation in dissolving rocks and other types of experiments or field observations that involve fingered growth. Common for all of these examples, and for the model, is that the growth of the interface is concentrated at the tips of long, thin fingers. There is a growth competition between the fingers, with the longer ones growing faster than the shorter ones, leading to a broad distribution of finger lengths.

Contents

1 Introduction **1**

2 Moving-boundary processes **5**
2.1 Solidification 5
2.2 Viscous fingering 7
2.3 Electrochemical deposition 9
2.4 Bacterial colonies 11

3 Fractals **13**
3.1 Self-similarity 14
3.2 Fractal dimension 15
3.2.1 The Richardson approach 16
3.2.2 The box-counting dimension 17
3.2.3 Radius of gyration 18

4 Mathematical description **19**
4.1 Conformal maps 20
4.2 Conformal invariance 21
4.3 The Riemann mapping theorem 22
4.4 Laurent expansions 23
4.5 Conformal equivalence and the composition property 23

5 Laplacian growth **26**
5.1 The Darcy flow law 27
5.2 Surface tension 29

6 Instabilities **31**
6.1 Mullins-Sekerka instability on a circle 32
6.2 Saffman-Taylor fingering 35

7 Growth models in radial geometry **38**
7.1 Continuous Laplacian growth 38
7.2 Pole dynamics 41
7.3 Diffusion-Limited Aggregation 42
7.4 Iterated maps 45
7.5 Conformal radius and fractal dimension 50
7.6 Iterated maps in the continuous limit 51

8 Loewner evolution **56**
8.1 The Loewner equation 56
8.2 Example: a growing stick 59
8.3 Numerical procedure 59
8.4 The Loewner equation for radial Laplacian growth 63

9 Fingered growth **65**
9.1 A model for fingered growth 66
9.2 Fingered growth in the half-plane 70
9.3 Fingered growth in channel geometry 74
9.4 Comments on numerics 77

10 Critical phenomena **80**
10.1 Scaling and universality 81
10.2 Conformal invariance 81
10.3 Stochastic Loewner Evolution 82

11 Summary **85**

A Derivation of the conformal map $f(\omega)$ **87**
A.1 Gauss' theorem 87
A.2 The Green's Function 89
A.3 The Green's function of a circle 90
A.4 The variation formula 91
A.5 Green's functions and maps 92

Bibliography **94**

Chapter 1

Introduction

Nature confronts us with patterns and pattern forming processes in a wide variety of contexts, such as frost on the car glass, branching of river networks, cauliflower, bacterial colonies and dendritic crystals in rocks. Most of these examples involve something irregular that has emerged (apparently) spontaneously from an initially smooth configuration. Fascinated by the beauty and complexity of these patterns, scientists have tried to explain the process behind their formation for centuries. The fact that most of the processes are non-equilibrium has complicated this work, but following the development and invention of new mathematical tools in physics, the patterns are continuously better understood. New models have been proposed that resemble what is observed in nature in great detail.

Hexagonal honeycomb and lamellar structures are examples of very simple, regular patterns. These stand in contrast to the complex nature of coastlines, dendrites and percolation patterns. Fascinatingly enough, the complex patterns can have surprisingly simple explanations and mechanisms behind them, and vice versa. The regular patterns are often formed close to equilibrium, and can sometimes undergo a transition to more complicated structures as the system is driven further away from equilibrium. Some systems are extremely sensitive to changes in the growth conditions, leading to a great diversity of patterns forming from

Figure 1.1: Some examples of the variety of patterns that can be observed in nature. Clockwise from top left: cross section of cauliflower, manganese oxides in rock, a bacterial network and frost on glass (from www.superstock.com; Rui Nunes, www.mindat.org; www.nd.edu/ malber; www.snowcrystals.com).

the same main process.

Most patterns in nature are formed due to interactions between thermodynamic properties, instabilities and transport processes. Convection, diffusion and advection will, in general, give different types of patterns. Typically, convection is the dominating transport process. However, in some well studied natural examples (such as mineral dendrites in rock and ice crystals on glass) convection simply cannot occur, in which case diffusion usually takes over control. The patterns that emerge by these kinds of processes are well described by several models.

A nice example of a pattern emerging from an initially smooth configuration is the snowflake. Starting out from a spherical frozen water droplet, it evolves into a complex crystal on its way through the atmosphere. The six branches forming due to the hexagonal structure of ice are similar to each other, but never identical, which is neatly illustrated in Fig. 1.2. The similarity arises because every branch grows under the same overall conditions: the temperature, pressure and humidity surrounding the crystal are the same at a particular instant. The differences occur due to impurities on the surface, leading to instabilities in the growth of the crystal at that point and subsequent evolution of a structure that slightly deviates from the other branches. The theory of solidification and pattern formation is an attempt to understand how a pattern can emerge from a smooth initial condition, and why it is so sensitive to microscopic impurities or perturbations.

Figure 1.2: The photo shows how the six branches of an ice crystal, grown under the same overall thermodynamic conditions, are similar but not identical. The differences occur because of small impurities and disturbances of the solid surface during the crystal growth (www.snowcrystals.com).

Chapter 2

Moving-boundary processes

Many of the patterns observed in nature can be described in terms of a surface that is moving due to external transport processes and properties of the surface itself. In the most simple examples, this external transport process can be described by a scalar field which satisfies the diffusion or Laplace equation. The boundary as a whole is moving due to gradients in this field, whereas a particular pattern is formed only if some of the impurities on the surface are unstable under the ruling conditions. The kinetics of the moving boundary are also sensitive to such impurities, and play an important role for the resulting pattern.

2.1 Solidification

Solidification is one of the simplest examples of a pattern forming process and is therefore well studied. It is controlled by the diffusion of either heat or mass, or by a combination of these. In the case of thermal diffusion, a solid is growing from a small seed particle that is immersed in an undercooled melt of the pure material. In the chemical analogue, the seed particle is growing from a supersaturated solution. Mathematically, both processes are described by a dimensionless scalar field U that represents

the temperature or concentration. U satisfies the diffusion equation

$$\mathcal{D}\nabla^2 U = \frac{\partial U}{\partial t}, \tag{2.1}$$

where $\mathcal{D}$ is the diffusion constant relevant for the process.

In the heat controlled problem, the surface temperature is not equal everywhere to the melting temperature T_m, due to some local thermodynamic effects and surface geometry. To obtain a correct solution of the problem, the thermodynamic boundary condition (frequently called the Gibbs-Thomson relation) [Langer, 1980]

$$T_{eq} = T_m(1 - \frac{\Upsilon\kappa}{L}) \tag{2.2}$$

has to be used for the equilibrium temperature of the curved surface T_{eq}. Here, Υ is the surface tension, κ is the curvature of the surface and L is the latent heat of solidification. These two equations introduce some of the most important parameters that control the process: Υ and κ are properties of the surface which are important for the pattern morphology. L and $\mathcal{D}$ together describe the heat flow during the solidification: L is the amount of heat generated at the phase boundary, whereas $\mathcal{D}$ decides how fast this heat can be transported away from the surface, and hence at which speed the solidification front can advance. If the phase transition produces much more heat than what can be transported away, the temperature at the phase boundary will increase and hence no more solidification will take place until the excess heat has diffused away from the surface.

In the chemically controlled problem, in which U represents a concentration field, a similar thermodynamic boundary condition needs to be taken into account. The chemical potential at a curved solid interface is higher than at a flat interface, leading to a solute concentration at the surface

$$C_s = C_0(1 + \frac{\Upsilon\kappa\mathscr{V}}{\mathscr{R}T}). \tag{2.3}$$

Here, C_0 is the concentration at equilibrium with a flat interface (for which $\kappa = 0$), $\mathscr{R}$ is the gas constant, T is the temperature and $\mathscr{V}$ is the molar

volume of the relevant material. The effect of this boundary condition is analogous to what was discussed for the thermal case.

When it comes to practical situations in material science, most processes of interest involve both thermal and chemical diffusion. One example is solidification of impure materials: The growth is controlled by the amount of heat generated at the phase boundary, and how fast impurities can be transported away from the surface. It is worth noting that thermal diffusion constants in general are much larger than chemical ones, thus the two effects will be important on two different length- and timescales.

The patterns that are formed in solidification processes are often categorised as dendrites. A dentritic pattern is characterised by its tree-like form with several generations of branching. The manganese oxides and frost crystals in Fig. 1.1 are typical examples of dendritic structures.

2.2 Viscous fingering

The most common example of Laplacian growth is viscous fingering in a Hele-Shaw cell, which is well studied and has contributed significantly to the increasingly better understanding of pattern-forming processes. A Hele-Shaw cell consists of two closely spaced parallel plates, usually made of glass. It is very useful when doing experiments in a two-dimensional geometry, either horizontally or vertically. Material can be added at one or more sides of the cell or from inlets in the middle of the plates. The motion of fluids in a Hele-Shaw cell is mathematically analogous to two-dimensional flow in a porous medium, which is of importance in oil industry.

Viscous fingering occurs when a horizontal Hele-Shaw cell is filled with an incompressible viscous fluid, such as oil. A less viscous, incompressible fluid (e.g water or air) is then added from an inlet in the middle of one of the plates. The latter fluid will displace the oil and make a pattern similar to the one seen in Fig. 2.1. The characteristics of the final

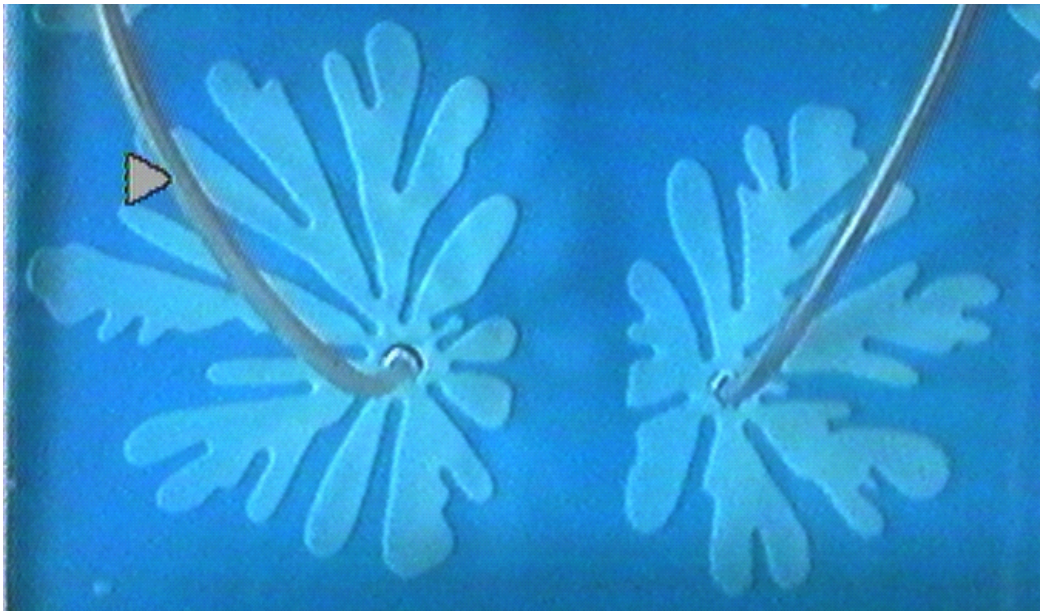

Figure 2.1: An example of a viscous fingering experiment. The image shows the characteristic morphology of such a pattern, together with the competition effect that will occur when the less viscous fluid is added from two sources simultaneously. From http://physics.unipune.ernet.in/∼agb/

pattern will be dependent on the source flux and viscosity ratio of the two fluids. Viscous fingering can be described in terms of the Saffman-Taylor instability, which will be discussed in Sec. 6.2.

2.3 Electrochemical deposition

Electrochemical deposition (ECD) is a diffusion-limited process that takes place during electrolysis. An electrolytic cell consists of two electrodes immersed in an electrolyte, which usually is a solution of ions in water. When an external voltage is applied to the electrodes, the ions in the electrolyte will seek towards the electrodes, where redox reactions will take place. The electrodes are called anode and cathode. The anode is the one that attracts anions (negatively charged ions) and the cathode attracts cations (positively charged ions). When an anion reaches the anode, it will oxidize by depositing electron(s) there. This will lead to the formation of a layer of oxidized anoins on the anode. Likewise, the cations will be reduced by reacting with electrons at the cathode. This way, a metal deposit may be formed at one or both of the electrodes, depending on the properties of the electrolyte. Brady and Ball did experiments in which they observed that the current between the electrodes was independent on the applied voltage [Brady and Ball, 1984]. This led them to the conclusion that the process is limited by diffusion and not controlled by any other mechanism. As soon as ions have reacted at one of the electrodes, there will be a concentration gradient in the electrolyte, leading to the diffusion of new ions towards the electrodes.

During the first decade after the work of Brady and Ball, much work was devoted to ECD experiments. It was considered a paradigm for the studies of non-equilibrium growth phenomena, due to the wide variety of morphologies that could be obtained [Kuhn and Argoul, 1994]. Different types and concentrations of ions, current densities and cell geometries would, in general, lead to structures of various characteristics. In order to properly study the peculiarities of the patterns obtained for different

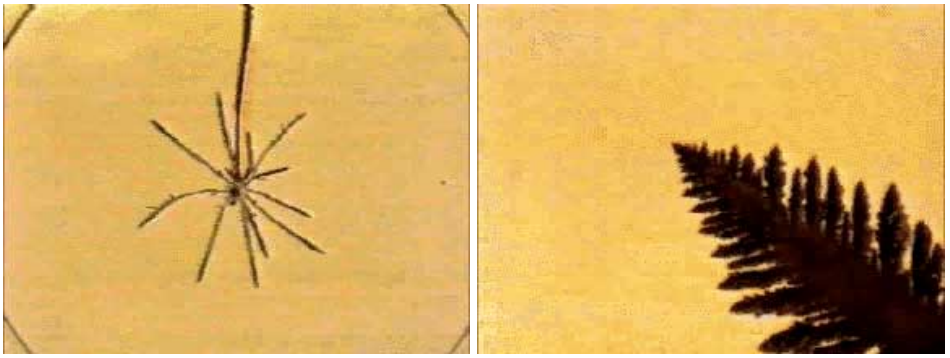

(a) (b)

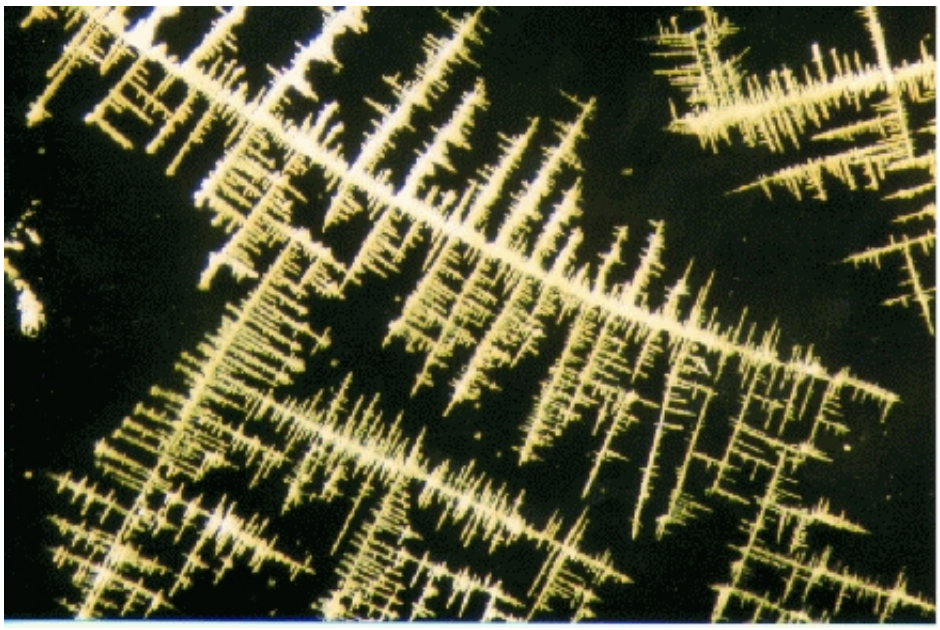

(c)

Figure 2.2: Two electrochemical deposition experiments. (a) shows the aggregate formed when the electrolyte is a zinc sulfate solution. The positive terminal is a circular loop centered at the point which is the negative terminal. The thickness of the loop wire, 0.5 cm, is the vertical spatial restriction of the experiment. The loop is of the order of centimeters in diameter. (b) shows a close-up of one of the zinc dendrites formed in (a). It has several generations of side branches, characteristic for dendritic structures. (c) A lead dendrite formed in a directional thin-layer electrodeposition experiment. Note how the morphology of these dendrites is qualitatively different from what is observed in (b). http://polymer.bu.edu/ogaf/ and http://www.qf.ub.es/d1/marta/morpho.html.

parameters, such studies are usually done in two-dimensional settings, which is obtained by sandwiching the electrolyte between two glass plates. All the images shown in Fig. 2.2 are examples of such spatially restricted experiments.

The most common ions used in ECD experiments are zinc, copper, tin, lead and iron. These will, in general, give branched dendrites with a wide range of different morphologies.

2.4 Bacterial colonies

The growth of bacterial colonies is another example of a diffusion-limited process that can lead to a great diversity of patterns. The properties of the final structure will be a function of the bacterial species and its growth conditions such as nutrient concentration and cell mobility. The classification of the colonies can be done in several different ways, but the simplest may be to divide them into two groups:

- colonies grown under limited nutrient supply. The evolution is controlled by the diffusion of nutrients towards the boundary of the colony. There will be a competition for the incoming flux, leading to a branched structure (Figs. 2.3(a) and 2.3(b)) with effective screening of the innermost parts

- colonies that always grow with sufficient amounts of nutrients available. Their growth is limited by how fast waste material produced by the bacteria themselves can diffuse away from the boundary. The results are different disc shaped structures, such as the one seen in Fig. 2.3(c)

The advantage in using bacteria in the study of pattern formation is that the growth conditions are easily varied and controlled, and the response to these changes can be observed on reasonable time scales. In contrast to other types of pattern formation experiments, growth of bacterial colonies in the laboratory offers the opportunity to observe the

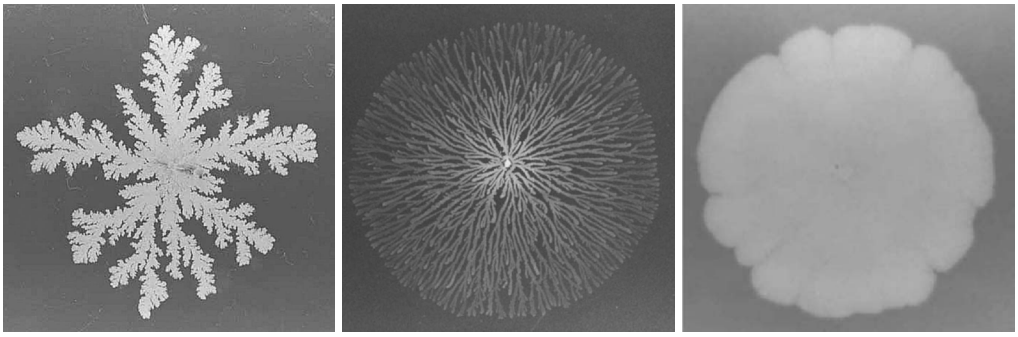

(a) (b) (c)

Figure 2.3: The images show examples of colonies of the bacterium Bacillus subtilis, grown under different conditions. (a) is a structure obtained when the bacteria grow on a hard substrate (which leads to limited cell motion and only local interaction between the cells) and with limited availability of nutrients. The pattern is very similar to the ones produced by the theoretical diffusion-limited aggregation (DLA) model, presented in Sec. 7.3. The colony in (b) is grown with the same low nutrient concentration but on a much softer substrate than in (a). The cells have more freedom to move towards the nutrients, leading to a more uniform density of branches. (c) shows the result of growth on a hard substrate but with a high concentration of nutrients. The branches in the pattern in (a) fuses into a compact disc shaped structure with a rough surface. The cells are growing fast due to the lucrative nutrition condutions, but are at the same time strongly bound to each other because of the hard substrate, forming a dense structure. [Matsushita et al., 2004]

structure and motion of individual cells. The coupling between this microscale behaviour and the macroscopic colony growth is important for the understanding of pattern forming processes in general [Matsushita et al., 2004].

Chapter 3

Fractals

When studying patterns, it soon becomes clear that classical Euclidian geometry is not a useful tool to describe what is observed. In fact, this is true for many of the shapes that surround us in nature. Benoît Mandelbrot descriptively wrote that "clouds are not spheres, mountains are not cones, coastlines are not circles" [Mandelbrot, 1982]. He then introduced the term *fractal* to classify these structures that were so complicated and complex that Eucledian geometry came up short in describing them.

The term fractal is constructed from the latin words for fragmented and irregular. The shapes that Mandelbrot wanted to describe had these two properties, and he found the expression useful for his purposes. As a definition of the term, he stated that "a fractal is a set for which the Hausdorff dimension strictly exceeds the topological dimension". This definition is somewhat theoretical, and it turns out that fractals have many other features in common that can be used to describe what they really are. Despite the fact that they are irregular and fragmented and cannot easily be described in terms of Euclidian geometry, they usually have a simple and recursive definition. They are self-similar and have a fine structure at arbitrary small scales. Furthermore, they can to a large extent be described by statistics.

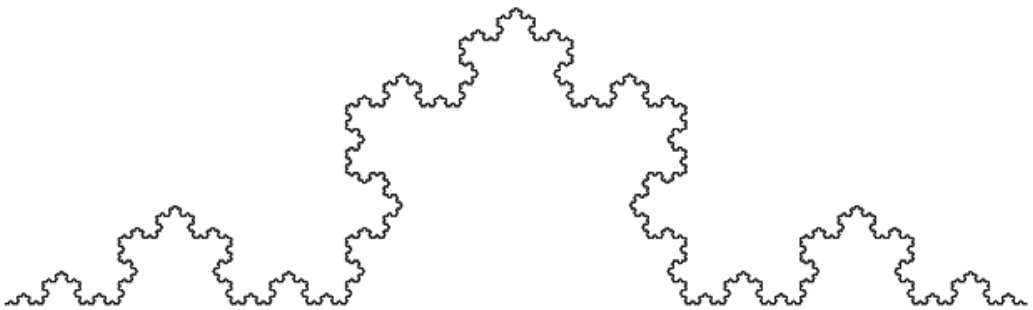

Figure 3.1: The Koch curve is a nice example of an exact self-similar fractal curve. It consists of straight lines of which the middle $\frac{1}{3}$ is replaced by a hat made out of two $\frac{1}{3}$-long line segments. Repeating this process indefinitely produces the curve shown in the figure. Observe that if the leftmost $\frac{1}{3}$ of the curve in the figure is magnified by a factor 3, the original curve is reproduced exactly. This is true for any part of the curve and at any length scale, which is the meaning of exact self-similarity.

3.1 Self-similarity

A self-similar structure shows similarities to itself, either exactly or statistically, on all scales. Any part of the shape looks the same as the whole shape. An example of an exact self-similar structure is the Koch curve in Fig. 3.1. By picking out an arbitrary part of it and rescaling it to the size of the whole curve, one reproduces something that looks exactly like the original structure. This can be done infinitely many times. An automatic consequence of this self-similar property is that all fractals have a fine structure at arbitrary small scales.

Statistical self-similarity refers to structures that on average will look the same when this rescaling is done. A common example is coastlines. A whole coastline will have a certain coarseness in its statistical description. If the whole coast of Norway is to be included in one image, only a certain number of islands and fjords can be distinguished. Upon rescaling with an arbitrary magnification factor, new islands and fjords will show up. Thus any fraction of the coastline will have the same statistics on average as the whole of it.

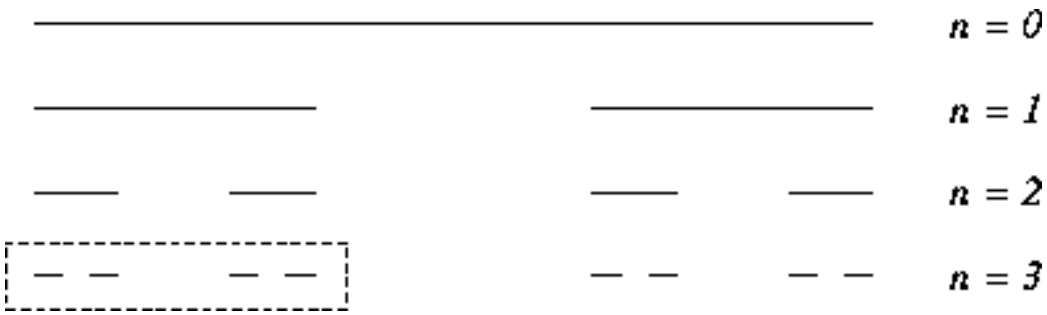

Figure 3.2: The Cantor set is perhaps the simplest fractal structure constructed by mathematicians. When going from one generation to the next, the middle $\frac{1}{3}$ of each line segment is removed. If the procedure is continued such that $n \to \infty$, the total length of the curve converges as $(\frac{2}{3})^n \to 0$. This leads to a paradox: the curve has infinitely many line segments, but the total length of all of these segments is zero.

Note that not all self-similar structures are fractals: the real line obeys self-similarity in addition to having a simple and recursive description. It is not very irregular though, and can easily be described in terms of Euclidean geometry. Hence, it fails to be a fractal despite the fact that it obeys some of the properties of fractals.

3.2 Fractal dimension

At the beginning of the 19th century, mathematicians realised that fragmented and irregular structures could not be described satisfactorily by the number of coordinates, which corresponds to the topological dimension. The fractal or Hausdorff dimension was then introduced as a way to describe to which extent a structure fills space. The Cantor set in Fig. 3.2 has infinitely many infinitesimal segments as the generation $n \to \infty$. Topologically it has dimension zero, because the segments are infinitesimal. But there are infinitely many of these segments, leading to the fact that the set fills more of space than only a single point (which is the topological meaning of dimension zero). As is seen in Fig. 3.2, the set is a subset of a line, so it does not fill enough space to be one-dimensional.

It will be shown that the Hausdorff dimension $\mathscr{D}_H$ of the Cantor set is $\frac{\log 2}{\log 3} \approx 0.6309$.

The same idea applies to Brownian motion, which is the random walk that a particle will make when it is suspended in a fluid. The trace of a random walker is a fractal curve: if the particle is allowed to walk around in the fluid for an infinitely long time, it will eventually visit every point in the body that contains the fluid. Its trace will then fill this space, and the topologically one-dimensional curve will have a Hausdorff dimension close to three. According to the definition given by Mandelbrot, it is therefore a fractal.

The real line is, as already mentioned, not a fractal: both $\mathscr{D}_H$ and the topological dimension $\mathscr{D}_T$ are equal to one. Any structure with non-integer $\mathscr{D}_H$ is a fractal, but there are examples of fractals with integer $\mathscr{D}_H$.

Depending on how the fractal is generated, the procedure for finding the fractal dimension will be somewhat different. For deterministic fractals as the Cantor set and the Koch curve, $\mathscr{D}_H$ can be found analytically. There are many ways to generate fractals though, and not all of them are as easy to handle as these two examples. Fractals can also be the result of stochastic processes, such as Brownian motion, and can be seen everywhere in nature. If a deterministic description is lacking, the fractal dimension has to be obtained empirically or numerically.

3.2.1 The Richardson approach

From empirical studies of the British coastline, L. F. Richardson found the relation $l(\delta) \sim \delta^{1-\mathscr{D}_R}$ for the length l of the coastline when it was measured by a yardstick of length δ. This result was published in an appendix to General Systems Yearbook in 1961. Mandelbrot adopted this relation, and argued that for fractal curves the $\mathscr{D}_R$ found by Richardson corresponded to $\mathscr{D}_H$.

The Cantor set in Fig. 3.2 is a simple example. When going from generation n to $n+1$, each line segment is rescaled by a factor $\frac{1}{3}$, and the

curve in $n+1$ covers $\frac{2}{3}$ of the curve in generation n:

$$l(\frac{\delta}{3}) = \frac{2}{3}l(\delta).$$

Now, inserting the relation found by Richardson leads to

$$(\frac{\delta}{3})^{1-\mathscr{D}_R} = \frac{2}{3}\delta^{1-\mathscr{D}_R}$$

$$\mathscr{D}_R = \frac{\log 2}{\log 3} \approx 0.6309.$$

For the Koch curve, the same derivation yields

$$l(\frac{\delta}{3}) = \frac{4}{3}l(\delta)$$

$$\mathscr{D}_R = \frac{\log 4}{\log 3} \approx 1.2618.$$

3.2.2 The box-counting dimension

Another approach to obtaining the fractal dimension of a set is by the box-counting method. The idea is similar to what Richardson did when working on coastlines, but when using box-counting one is no longer restricted to the one-dimensional yardstick. The fractal curve or set is placed on an evenly spaced grid. The number N of grid cells or boxes needed to cover the set is dependent on the grid spacing or box side length δ. The box-counting dimension $\mathscr{D}_B$, which is also referred to as the Minkowski-Bouligand dimension, is obtained from the relation $N(\delta) = \delta^{-\mathscr{D}_B}$. Strictly speaking, $\mathscr{D}_B$ is found by studying the behaviour of $N(\delta)$ as δ gets smaller, leading to the more formal definition

$$\mathscr{D}_B(\delta) = \lim_{\epsilon \to 0} \frac{\log N(\delta)}{\log \frac{1}{\delta}}.$$

The box-counting method is frequently used to calculate the fractal dimension of computer-generated sets.

3.2.3 Radius of gyration

The radius of gyration $\mathcal{R}_g$ is another useful tool for obtaining a fractal dimension measurement for digitised structures. $\mathcal{R}_g$ is the root mean square distance of the parts of a cluster from its center of gravity $\mathcal{R}_C = \frac{\Sigma_{j=1}^{N} r_j}{N}$. r_j is the position of the jth site or grid point of the digitised structure, with respect to the origin. If the fractal was to be rotated around an axis through $\mathcal{R}_C$, then the kinetic energy and angular momentum of this motion would be the same as if all of the grid points were placed on a circular ring of radius $\mathcal{R}_g$ centered at $\mathcal{R}_C$.

The radius of gyration can be computed by the two equivalent relations

$$\mathcal{R}_g^2 = \frac{\Sigma_{j=1}^{N} |r_j - \mathcal{R}_C|^2}{N} = \frac{\Sigma_{j,i} |r_j - r_i|^2}{2N^2}, \tag{3.1}$$

where the last is the average distance between two sites. Now it may be shown [Stauffer, 1985] that $\mathcal{R}_g$ is related to the number of sites and a fractal dimension $\mathscr{D}_g$ by

$$N \sim \mathcal{R}_g^{\mathscr{D}_g} \tag{3.2}$$

The $\mathscr{D}_g$ obtained from Eq. (3.2) is also used as a description of irregular structures that are not self-similar and hence, strictly, are not fractals. Examples are percolation clusters away from the percolation threshold.

Chapter 4

Mathematical description

Even though patterns arise due to a wide variety of physical processes and thus can look very different, the framework of their mathematical description is the same. The basic concepts and theoretical background will be introduced here.

The discussion is restricted to two-dimensional processes, and in doing so, the connection to the real world is not lost: frost on glass and ice crystals growing in the atmosphere are examples of two-dimensional patterns in nature, in addition to viscous fingering and other patterns that can be constructed under spatial restrictions in the lab. The two-dimensional mathematical description is convenient to work with, easy to visualise, and even turns out to reproduce what is observed in nature. In two dimensions a point can be represented by a complex number $z = x + iy$, and all the techniques of complex analysis can be applied. The close resemblence between complex function theory and geometrical shapes is the key to the usefulness of complex numbers for these purposes. The fact that the two-dimensional information (x, y) can be stored in one variable z, without loss of information, makes complex numbers especially convenient to work with.

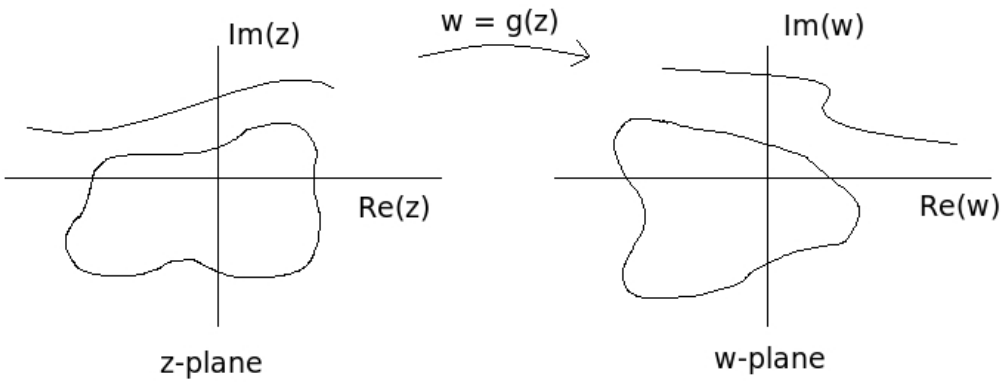

Figure 4.1: The graphing procedure of functions of complex variables uses two planes to illustrate the correspondence between the four variables $x =$ Re(z), $y =$Im(z), $u =$Re(ω) and $v =$Im(ω). Both single points, curves and domains can be mapped by the function $\omega = g(z)$.

4.1 Conformal maps

In real analysis, a function $y = g(x)$ can be presented graphically in the xy-plane, as $g(x)$ assignes a y-value to every value of x. In complex analysis, where every point is represented by the variable $z = x + iy$, this graphing procedure is no longer applicable. The function $\omega = u(x, y) + iv(x, y) = g(z)$ involves a correspondence between the four variables x, y, u and v, and the conventional graphing procedure would require using a four-dimensional space. To avoid the inconvenience this would include, graphing in complex analysis is rather done using two planes: the z-plane and the ω-plane. The procedure is illustrated in Fig. 4.1. The function $\omega = g(z)$ maps the points $z = x + iy$ in the z-plane onto the corresponding $\omega = u + iv$ in the ω-plane. Not only points, but also curves as well as whole domains can be mapped between the z- and ω-plane.

If the mapping $\omega = g(z)$ preserves angles, it belongs to a family called conformal maps. More precisely, a map that is conformal at z_0 preserves the size and orientation of the angle between any two curves through z_0. It turns out that if $g(z)$ is analytic in a domain D (which means that it has

derivatives of all orders throughout D), then $g(z)$ is conformal at every point in D where its first derivative is not equal to zero. The nonzero derivative implies that different points in D are mapped to different points in the ω-plane. It can be shown that if a mapping is conformal at a point z_0, then it has a local inverse there.

4.2 Conformal invariance

The conformal invariance property of harmonic functions is the key to why conformal maps are so useful in the study of moving-boundary processes in Laplacian fields. Take the function $\omega = g(z)$ that maps the domain D_z in the z-plane conformally onto the domain D_ω in the ω-plane. Let $\Phi(z)$ be harmonic in D_z, that is: $\Delta_z \Phi(z) = \nabla_z \nabla_{z^*} \Phi(z) = 0$. $\nabla_z = \frac{\partial}{\partial x} + i\frac{\partial}{\partial y}$ is the complex gradient in the z-plane, and $\nabla_{z^*} = \frac{\partial}{\partial x} - i\frac{\partial}{\partial y}$ is its conjugate. When $\Phi(z)$ is mapped to D_ω by $g(z)$, it must satisfy

$$\frac{\partial \Phi(\omega)}{\partial \omega} = \frac{\partial \Phi(g(z))}{\partial \omega} = \frac{\partial \Phi(g(z))}{\partial g(z)} \frac{\partial g(z)}{\partial z} \frac{\partial z}{\partial \omega} = \frac{\partial \Phi(z)}{\partial z} \left(\frac{\partial g}{\partial z} \right)^{-1}.$$

This can be used to show the relations

$$\frac{\partial}{\partial z} \frac{\partial}{\partial z^*} \Phi(z) = \left(\frac{\partial g}{\partial z} \right) \left(\frac{\partial g}{\partial z} \right)^* \frac{\partial}{\partial \omega} \frac{\partial}{\partial \omega^*} \Phi(\omega);$$

$$\Delta_z \Phi(z) = \left| \frac{\partial g}{\partial z} \right|^2 \Delta_\omega \Phi(\omega). \tag{4.1}$$

Now $g(z)$ is a conformal map, which means that its derivative $\frac{\partial g}{\partial z}$ is nonzero. Considering the fact that $\Phi(z)$ is harmonic in D_z, which means that the left-hand side of Eq. (4.1) is zero, it follows that $\Delta_\omega \Phi(\omega) = 0$. In other words: if a domain can be reached by a conformal map of another domain, then a function that is harmonic in one of the domains automatically must be harmonic in both domains.

Many basic equations in physics involve harmonic functions, such as electromagnetic and gravitational fields. The conformal invariance

property makes conformal maps a useful tool in these applications.

4.3 The Riemann mapping theorem

The usefulness of conformal maps becomes even more evident when introducing further properties: The Riemann mapping theorem states that for any simply connected domain D (i.e. the boundary of the domain is a single closed curve, and there are no points inside this curve that do not belong to D) in the z-plane, which is not the entire z-plane, there exists a unique conformal map $\omega = g(z)$ that brings D onto the unit disc, and that transforms the boundary of D into the unit circle.

Even though not stated explicitly, the Riemann mapping theorem implies that by combining conformal maps, it is possible to find the map between any two domains that satisfy the restrictions given in the theorem. This stems from the fact that when $g(z)$ is conformal in D, it is also invertible there. That is, if $g_1(z)$ maps the domain D_1 onto the unit disc, and $g_2(z)$ does the same to D_2, then the composition $g_2^{-1}(g_1(z))$ maps D_1 directly onto D_2 (g_2^{-1} is the inverse of g_2, which means that $g_2^{-1}(g_2(z)) = z$). As a consequence, one is not restricted to the unit disc or the physical plane when dealing with Laplacian fields. When working with a problem that is described by an harmonic function, the treatment may be complicated if its geometry is inconvenient in the physical plane. If it is possible to find a domain where the geometry of the problem makes it simpler to solve, then the Riemann mapping theorem guarantees that there will be a conformal map that can take the harmonic function there.

The only restriction to take care of when mapping harmonic functions between different domains, is that the boundary conditions must also be conformally invariant. This is true if

- the value of the harmonic function Φ at the boundary, or eventually the jump in its value across the boundary, is a constant
- the normal derivative of Φ at the boundary is zero.

These are special cases of Dirichlet and Neumann boundary conditions, respectively. Most other boundary conditions are not conformally invariant [Bazant and Crowdy, 2005].

4.4 Laurent expansions

It has already been stated that a function which is analytic in a domain D has derivatives of all orders there. This can be used to show that if the function $g(z)$ is analytic in D, then it can be written as the sum of a convergent power series in a neighbourhood of each point z_0 in D: $g(z) = \sum_{j=0}^{\infty} c_j (z - z_0)^j$. The coefficients c_j are real numbers. This representation only contains positive powers of z. A two-sided power series of the form $g(z) = \sum_{j=-\infty}^{\infty} c_j (z - z_0)^j$ is valid if $g(z)$ is analytic in an annulus $\mathcal{R}_1 < |z - z_0| < \mathcal{R}_2$. This representation is called a Laurent expansion and can be useful when working in domains that contain the point at infinity. The radius $\mathcal{R}_1$ cannot be zero, but $\mathcal{R}_2$ may be infinite. A conformal map can therefore always be represented by a power series, either in positive powers or as a Laurent series, depending on the domain in which it is conformal. The series expansion is unique, and the coefficients c_j are determined by important properties such as the boundary conditions of the map.

4.5 Conformal equivalence and the composition property

In Sec. 4.3 it was shown that there exists a conformal mapping between any two simply connected domains that are subsets of the complex plane. If there exists a conformal mapping of D_1 onto D_2, then D_1 and D_2 are said to be conformally equivalent. That is, the conformal mapping between the two must satisfy the usual axioms of an equivalence relation: reflexivity, symmetry and transitivity. The transitive property implies that the composition of two conformal mappings is also a conformal mapping.

This property turns out to be especially useful when dealing with moving boundaries and pattern forming processes, and it will be used thoroughly in the Chapters 7 - 9. In fact, every conformal map is a composition of local rotation, translation and magnification [Fogedby, 2007].

When applying conformal maps to moving boundaries, growing domains and pattern forming processes, the idea goes like this: a reference domain is chosen in such a way that the problem at hand is nice to handle in that geometry. Examples of reference domains are the unit disc, the exterior of the unit circle, or the upper half-plane. Then the conformal map between the domain D in physical space (say, the z-plane, see Fig. 4.2) and the reference domain R (which lies in the mathematical ω-plane) is found. Now the evolution of D can be studied by mapping it to R, imposing controlled changes there, and then applying the inverse map back to the z-plane to study what the real effects of the changes will be in physical space. As an example, let $\omega = g(z)$ be the mapping of D onto R, and let $f(\omega)$ be its inverse. If $h(\omega)$ represents a small perturbation or growth of R, then $f(h(\omega))$ is the composition of mappings that codes for how these changes affect the domain in the z-plane.

Another technique uses instead a fixed reference domain. This requires that the mapping $g(z)$ and hence also $f(\omega)$ must change whenever the structure in the z-plane changes. This is the idea behind Loewner evolution, which is used in Chapters 8 and 9.

Both techniques have their positive and negative sides, and there is typically a certain range of moving-boundary processes for which each of them is particularly useful.

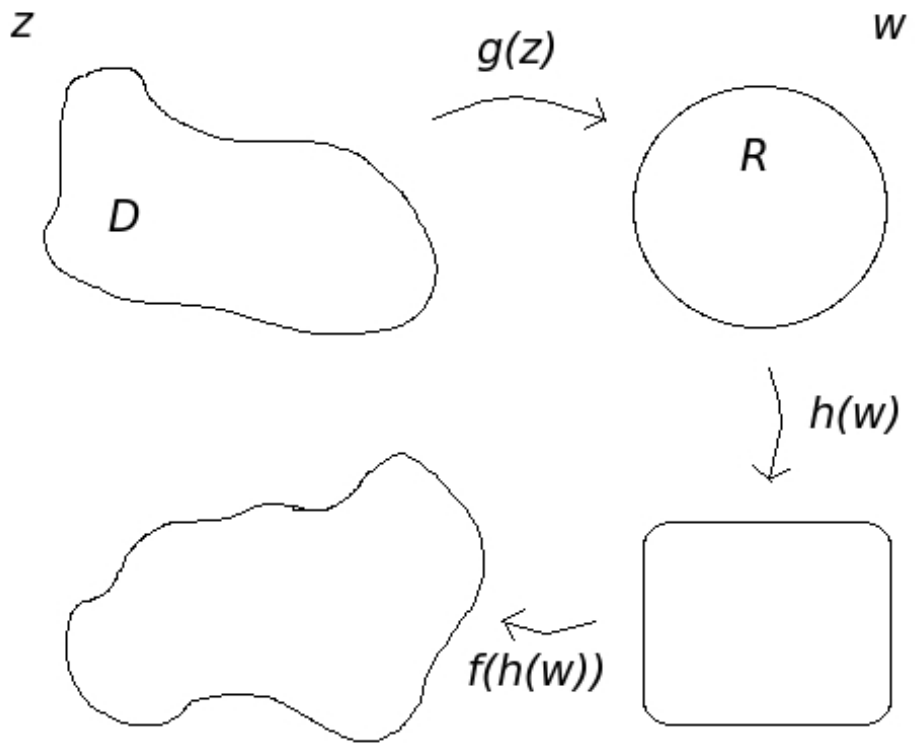

Figure 4.2: An illustration of how a reference domain R can be used to control and study the evolution of a structure D in physical space.

Chapter 5

Laplacian growth

Conformal maps can be used to study many of the moving-boundary processes presented in Chapter 2. Conformal invariance combined with the Riemann mapping theorem is the key to the usefulness of this technique, as will be made clear throughout this section. However, some important simplifications and approximations must be made before conformal mapping methods can be applied.

For growth problems that involve diffusion of temperature or mass in a fluid, the Péclet number Pe is an important parameter. It is defined as

$$Pe = \frac{\mathcal{L}V}{\mathcal{D}},$$

where $\mathcal{L}$ is a characteristic length and V is the velocity of the moving interface. $\mathcal{D}$ represents either the thermal diffusivity or the mass diffusion constant, depending on the process at hand. The Péclet number is proportional to the Reynolds number, and is a measurement of the stationarity of the growth. In the limit $Pe \ll 1$, the diffusion field is allowed to adjust to the changing shape of the interface, making the process quasistationary. This means that the time derivative in the diffusion equation can be omitted such that the growth is governed by the Laplace equation. This typically happens at low growth velocities, which in the solidification case is experienced at low undercooling or low supersaturation.

Viscous fingering is an example of a moving-boundary process that is governed by a pressure field rather than diffusion of heat or mass. Under certain circumstances, such processes can also be governed by a Laplacian field, which will be shown in Sec. 5.1.

Such processes fall into a category called Laplacian growth problems. Laplacian growth is viewed as a fundamental model for pattern formation. Its usefulness stems from the fact that the harmonic field that controls the growth is conformally invariant, which means that it can be mapped from the growing structure onto any other simply-connected reference domain. The solution of the Laplace equation may easily be found in this mathematical reference domain, and hence the growth can be studied in a simple way, as described already in Sec. 4.5.

5.1 The Darcy flow law

In Laplacian growth problems, the relationship between the interface velocity and the harmonic field is described by Darcy's law. This fundamental law was proposed by Henri Darcy as an empirical relation describing fluid flow in a porous medium. It has later been derived from the Navier-Stokes equation, and shown to be applicable to other types of fluid flow aswell. Here, the equation will be derived for two immiscible viscous fluids, analogous to the viscous fingering example.

If the flow in the fluids has a very low Reynolds number, $Re \ll 1$, advective inertial forces are negligible compared to viscous forces. This happens for very small displacements, low fluid velocities v or very high viscosities μ. Under these circumstances, the Navier-Stokes equation can be simplified to

$$\mu \nabla^2 v + \mathbf{f} - \nabla p = 0, \tag{5.1}$$

which is called Stokes flow. p is the pressure in the fluids, whereas $\mathbf{f}$ represents the sum of all body forces and will be set to zero in this

derivation. Under the assumption that the fluids are incompressible:

$$\nabla \cdot v = 0, \tag{5.2}$$

then Eq. (5.1) simplifies to the Laplace equation for the pressure:

$$\Delta p = 0. \tag{5.3}$$

Let the two immiscible fluids be trapped in a horisontal Hele-Shaw cell with plate spacing b, where one of the fluids is a circular inclusion in the other (when the less viscous fluid is the inclusion, this is exactly the setup for viscous fingering). Choose coordinates in such a way that the fluids lie in the xy-direction, and the thickness of the cell is in the z-direction, with the fluids confined to the space between $z = 0$ and $z = b$.

Eqs. (5.2) and (5.3) are valid for three dimensions and are not automatically satisfied in this quasi-two-dimensional geometry. If one assumes that the velocity of the fluids vanish at the plates, that is: $v_z = 0$ at $z = 0$ and $z = b$, gap-averaging the incompressibility equation (5.2) across the plate spacing b gives

$$\frac{1}{b}\int_0^b \nabla \cdot v \, dz = \frac{\partial \hat{v}_x}{\partial x} + \frac{\partial \hat{v}_y}{\partial y} + \frac{v_z(b) - v_z(0)}{b} = \frac{\partial \hat{v}_x}{\partial x} + \frac{\partial \hat{v}_y}{\partial y}. \tag{5.4}$$

$\hat{v}_x$ and $\hat{v}_y$ are the gap averages of the velocitiy components in the x- and y-directions, respectively. Eq. (5.4) shows that the incompressibility assumption translates to the gap-averaged velocities such that Eq. (5.3) is valid also for this approxiamtion.

Assume further that the velocity components $v_x(x, y, z)$ and $v_y(x, y, z)$ have a parabolic dependence in the z-direction:

$$v_i(x, y, z) = -\nu_i z(z - b), \tag{5.5}$$

for $i = x, y$, where ν_i denotes a gap-averaged strength. This can be used

to find the gap averages of each component:

$$\hat{v}_i = \frac{1}{b}\int_0^b v_i(x,y,z)\,dz = -\frac{1}{b}\int_0^b \nu_i z(z-b)\,dz = \nu_i \frac{b^2}{6}. \tag{5.6}$$

In the next step, one may assume that $\frac{\partial^2 v_i}{\partial j^2} \ll \frac{\partial^2 v_i}{\partial z^2}$ for $j = x, y$, such that Eq. (5.1) simplifies to

$$\mu \frac{\partial^2 v}{\partial z^2} = \nabla p. \tag{5.7}$$

By inserting Eq. (5.5) into Eq. (5.7) and finally using Eq. (5.6), one arrives at the result

$$\nu = -\frac{1}{2\mu}\nabla p,$$

$$\hat{v} = -\frac{b^2}{12\mu}\nabla p, \tag{5.8}$$

which is valid in the directions parallel to the cell plates.

Note that this derivation does not take the effect of gravity into account, because the gravitational forces are directed in the z-direction and therefore does not affect the velocities in the x- and y-directions. For flow in a vertical Hele-Shaw cell, placed in the xz-plane, the derivation yields an equation similar to Eq. (5.8):

$$\hat{v} = -\frac{b^2}{12\mu}\nabla(p + \rho g z). \tag{5.9}$$

A gravity term has been added, in which ρ is the fluid density and g is the gravitational acceleration constant.

5.2 Surface tension

The Darcy law in Eq. (5.8) was derived for one special example. More generalised, the Laplacian growth model assumes that the normal velocity of the interface, V_n, is proportional to the field gradient at the interface to some exponent η:

$$V_n \sim |\nabla U|^\eta. \tag{5.10}$$

U is a Laplacian field that can represent pressure, temperature, mass or some other quantity, depending on the problem studied. If one assumes zero surface tension, the boundary condition at the interface is conformally invariant and conformal mapping techniques can be used to solve the problem.

Surface tension is introduced by the boundary condition $U(z_b) = \Upsilon\kappa$ for the points z_b at the interface between the two liquids. This boundary condition is not conformally invariant, which complicates the analysis considerably. Surface tension is only significant in the case of high curvature, i.e. for narrow fingers and sharp tips. From electromagnetism it is well known that the (harmonic) electrostatic potential around a sharp tip is infinitely strong. This is also true for the field U in Eq. (5.10). The growth velocity around thin fingers will therefore be very high, and surface tension is the only stabilising force that can oppose the rapid growth of the parts of the interface with high curvature. Saffman and Taylor showed that the effect of surface tension in Hele-Shaw cells was to limit instabilities in the growth to the fingers having a curvature smaller than a certain limit [Saffman and Taylor, 1958]. This has important effects on the final pattern, and it seems that the surface tension essentially selects the finger width. The Saffman-Taylor problem is presented in Sec. 6.2.

Chapter 6

Instabilities

An important ingredient in the study of pattern formation is the stability of the moving interface. The competition between stabilising and destabilising effects on the evolving boundary is important for the pattern selection and the emergence of a characteristic length scale of the structure. Finger width, branching and tip splitting, and interface morphology are characteristics that can be understood in terms of stability analysis. The basic idea is to determine the stability of the dynamical equation of the moving boundary with respect to a shape perturbation. Both Saffman and Taylor [Saffman and Taylor, 1958] and Mullins and Sekerka [Mullins and Sekerka, 1963], [Mullins and Sekerka, 1964] did pioneering work on linear stability analysis. Saffman and Taylor studied fluid-fluid interfaces and their results are relevant to classical problems such as viscous fingering. Mullins and Sekerka worked with solidification fronts and considered both spherical and planar surfaces undergoing growth controlled by thermal or chemical diffusion fields. Even though these simple, theoretical models are now superseded, they still represent a general approach to gaining basic insight into several different types of pattern-forming processes.

6.1 Mullins-Sekerka instability on a circle

The derivation of the stability of a slightly perturbed circle can be applied to problems such as Diffusion-Limited Aggregation (DLA, to be discussed in Sec. 7.3) [Witten and Sander, 1983], and moving solidification fronts controlled by the diffusion of heat or mass. This derivation treats one special case, but with some changes in boundary conditions it can be applied to other diffusional growth problems.

Consider a circular surface that is growing in a Laplacian field U, which in this example represents concentration. The normal velocity of the surface is proportional to the gradient of the local field, according to Eq. (5.10) (using $\eta = 1$). The circle has an original radius $\mathcal{R}_0$, and is deformed by a small perturbation $\epsilon \cos(m\theta)$, $m \geq 1$, such that the equation for the local radius $\mathcal{R}(\theta)$ of the circle reads

$$\mathcal{R}(\theta) = \mathcal{R}_0 + \epsilon \cos(m\theta), \tag{6.1}$$

where the amplitude of the perturbation is time dependent, $\epsilon = \epsilon(t)$, and initially small enough that second- and higher order terms can be neglected.

The equilibrium concentration $U_s(\theta)$ on the surface $\mathcal{R}(\theta)$ is given by Eq. (2.3) and reads $U_S(\theta) = U_0\left[1 + \Upsilon_C \kappa(\theta)\right]$, where the capillary constant $\Upsilon_C = \frac{\gamma \mathscr{V}}{\mathscr{R}T}$ has been introduced as an abbreviation. The curvature of an arc $s(\theta)$ that is parameterised in polar coordinates is given by

$$\kappa(\theta) = \frac{s^2(\theta) + 2(\frac{\partial s}{\partial \theta})^2 - s(\theta)\frac{\partial^2 s}{\partial \theta^2}}{\left(s^2(\theta) + (\frac{\partial s}{\partial \theta})^2\right)^{\frac{3}{2}}}$$

[do Carmo, 1976], which in the current example leads to

$$\kappa(\theta) = \frac{\mathcal{R}_0 + (m^2 - 1)\epsilon \cos(m\theta)}{\mathcal{R}_0^2}. \tag{6.2}$$

The boundary condition at the surface $\mathcal{R}(\theta)$ then reads

$$U_s(\theta) = U_0\Big(1 + \frac{\Upsilon_C}{\mathcal{R}_0^2}\left[\mathcal{R}_0 + (m^2-1)\epsilon\cos(m\theta)\right]\Big). \tag{6.3}$$

With r the distance from the center of the circle, the expression

$$U(r,\theta) = A\log r + \frac{B\epsilon\cos(m\theta)}{r^m} \tag{6.4}$$

is a solution of the Laplace equation, satisfying the boundary condition that the flux at infinity should be unaffected by the perturbation. The field around an unperturbed circle behaves like $U(r) \sim \log|r|$, which is therefore also how $U(r,\theta)$ in Eq. (6.4) must behave as $r \to \infty$. At the surface $\mathcal{R}(\theta)$, Eq. (6.4) reads

$$U(\mathcal{R}(\theta)) = A\log\mathcal{R}_0 + \epsilon\cos(m\theta)\left[\frac{A}{\mathcal{R}_0} + \frac{B}{\mathcal{R}_0^m}\right], \tag{6.5}$$

which must be equal to Eq. (6.3). A and B are determined by equating the coefficients of like harmonics in this boundary condition expression. The final result for the field U reads

$$U(r,\theta) = \frac{\log r}{\log\mathcal{R}_0}U_0\left(1 + \frac{\Upsilon_C}{\mathcal{R}_0}\right) \tag{6.6}$$

$$+\frac{\epsilon\cos(m\theta)\mathcal{R}_0^{m-2}U_0}{r^m}\left(\Upsilon_C(m^2-1) - \frac{\Upsilon_C+\mathcal{R}_0}{\log\mathcal{R}_0}\right).$$

The normal velocity of the interface is proportional to the gradient of Eq. (6.6). For small perturbations it is sufficient to consider the radial derivative of $U(r,\theta)$, which leads to

$$V_n = \frac{d\mathcal{R}_0}{dt} + \frac{d\epsilon}{dt}\cos(m\theta) = \left.\frac{\partial U(r,\theta)}{\partial r}\right|_{r=\mathcal{R}(\theta)}.$$

By again equating the coefficients of like harmonics, expressions for $\frac{d\mathcal{R}_0}{dt}$

and $\frac{d\epsilon}{dt}$ are found:

$$\frac{d\mathcal{R}_0}{dt} = \frac{U_0(\mathcal{R}_0 + \Upsilon_C)}{\mathcal{R}_0^2 \log \mathcal{R}_0} = \frac{U_\mathcal{R}}{\mathcal{R}_0 \log \mathcal{R}_0}, \tag{6.7}$$

$$\frac{1}{\epsilon}\frac{d\epsilon}{dt} = \frac{U_\mathcal{R}(m-1)}{\mathcal{R}_o^2 \log \mathcal{R}_0} - \frac{U_0 \Upsilon_C}{\mathcal{R}_0^3}(m^3 - m). \tag{6.8}$$

$U_\mathcal{R} = U_0(1 + \frac{\Upsilon_C}{\mathcal{R}_0})$ is the equilibrium concentration on an unperturbed circle, for which the curvature reads $\kappa = \frac{1}{\mathcal{R}_0}$.

Eq. (6.8) is the growth rate of the perturbation amplitude and consists of two parts: the last term is the capillary effect and the other is the gradient term. The capillary effect is proportional to Υ_C and the surface tension. It is negative and therefore it favours a decay of the perturbation. The gradient term is always positive and proportional to $U_\mathcal{R}$ and favours growth. In the absence of surface tension, the capillary effect vanishes and there is nothing to stabilise the surface. From Eq. (6.3) it is understood that the surface then takes on a uniform concentration, regardless of the shape. At the same time, it is known that the concentration at infinity is unaffected by any irregularities on the interface. This means that the change in concentration between the interface and infinity is everywhere the same, such that isoconcentration lines must be more densely packed above buldges than at depressions, as is illustrated in Fig. 6.1. This gives a steeper concentration gradient and larger surface velocity at protuberances, which causes buldges to grow unstably. This is the action of the gradient term.

Whenever surface tension is present, the capillary effect is opposing this instability. The curvature is positive for protuberances and negative for depressions, and it is larger in absolute value for small buldges than for large ones. From Eq. (6.3) it is clear that the concentration at the interface is nonuniform as long as Υ_C is nonzero, and that it is larger at buldges than at depressions. This will lead to a flow of material, within the solid, from protuberances and into depressions. Hence the amplitude of the perturbation will shrink, and the surface will reattain its original,

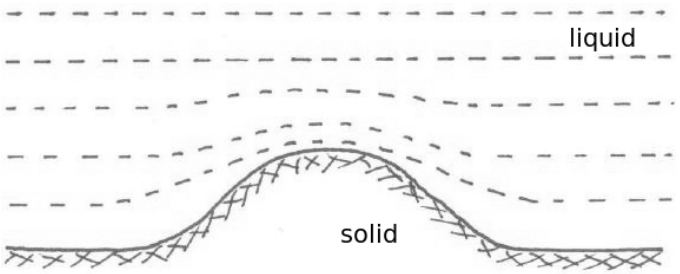

Figure 6.1: An illustration of how a buldge on the interface lead to a denser packing of the isoconcentration lines and thus a steeper field gradient.

circular and undistorted shape. This process is a part of nature's struggle towards a reduction in surface area and energy.

In general both effects will be present, and the stability of the surface will be determined by the competition between them.

6.2 Saffman-Taylor fingering

In 1958, Saffman and Taylor presented their pioneering work on the stability of fluid-fluid interfaces and it has since stood as the classical description of viscous fingering patterns [Saffman and Taylor, 1958]. Fig. 6.2 shows the result of a computer simulation of the equations they developed. They considered the setup where two fluids are confined to the narrow gap between a pair of closely spaced vertical plates, with one of the fluids displacing the other without mixing. The interface between the fluids moves with a constant velocity V vertically upwards. The coordinate system is chosen such that the plane $z = 0$ coincides with the moving unperturbed surface, whereas x is the horisontal coordinate along the interface. Now the fluid-fluid interface is perturbed by a function of the form $z = h(x,t) = \epsilon e^{imx+w(m)t}$. The fluid below the interface (fluid 1) is displacing the other (fluid 2), hence the velocity at the interface is goverened by gravity and a pressure field. For incompressible fluids, the fluid velocity v is assumed to be controlled by the Darcy law in Eq. (5.9),

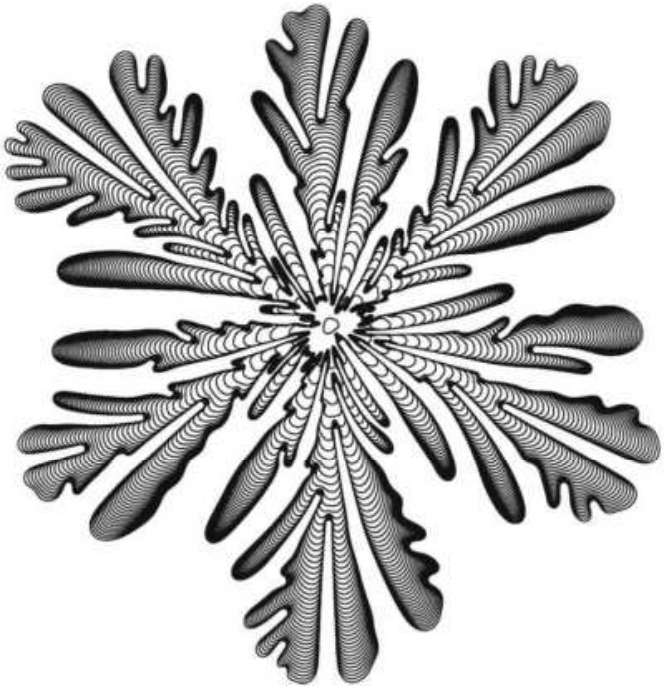

Figure 6.2: The figure shows the result of a computer simulation of the Saffman-Taylor instability, which is an attempt to describe viscous fingering patterns. Indeed, the structure is similar to the experimental viscous fingering pattern shown in Fig. 2.1. (adapted from J. Comp. Phys, 212, pp. 1-5 (2006)).

and is thus related to a Laplacian scalar field U by

$$v = -\frac{K}{\mu}\nabla(p + \rho g z) = \nabla U, \tag{6.9}$$

where K replaces $\frac{b^2}{12}$ as the fluid permeability of the Hele-Shaw cell. $\frac{\mu_i}{K_i}U_i = p + \rho_i g z$ is called the hydraulic potential of fluid i.

For the purpose of the analysis, it is assumed that the fluids are divided by a sharp interface, in contrast to an ill-defined transition region which more likely is the case. The effect of surface tension is neglected, such that the velocity and the pressure are continuous across the interface. It follows that at the interface $z = h(x, t)$, the condition

$$\frac{\partial U_1}{\partial z} = \frac{\partial U_2}{\partial z} = V + \epsilon w(m) e^{imx + w(m)t} \tag{6.10}$$

must be satisfied. The solutions of the Laplace equation that satisfy this boundary condition, in addition to the requirement that the field at infinity

should be unaffected by the perturbation, read

$$U_1 = Vz - \frac{\epsilon w(m)}{m} e^{imx - mz + w(m)t}, \tag{6.11}$$

$$U_2 = Vz + \frac{\epsilon w(m)}{m} e^{imx + mz + w(m)t}, \tag{6.12}$$

where the subscripts indicate to which fluid the potentials belong. The pressures, $p_1 = -\frac{\mu_1}{K_1} U_1 - \rho_1 g z$ and $p_2 = -\frac{\mu_2}{K_2} U_2 - \rho_2 g z$, must also be equal at the interface $z = h(x,t)$, leading to the relation

$$\frac{w(m)}{m}\left(\frac{\mu_1}{K_1} + \frac{\mu_2}{K_2}\right) = g(\rho_1 - \rho_2) + V\left(\frac{\mu_1}{K_1} - \frac{\mu_2}{K_2}\right). \tag{6.13}$$

The permeabilities, viscosities and m are always positive, which means that the sign of the right hand side of Eq. (6.13) codes for the sign of $w(m)$ and hence for the stability of the interface. If $w(m)$ is positive the perturbation will grow exponentially in time and the surface will be unstable to even small disturbances. On the other hand, if $w(m)$ is negative, any perturbation of the surface will exhibit an exponential decay and thus the interface will be stable. From the form of Eq. (6.13) it may be concluded that for sufficiently high velocities, the stability of the surface depends on whether the motion is towards or away from the less viscous fluid. If the less viscous fluid is displacing the more viscous one, then $\mu_2 > \mu_1$, $w(m)$ is negative and the interface will be unstable.

Chapter 7

Growth models in radial geometry

Many of the examples of growth processes have been studied in radial geometries, such as viscous fingering (Fig. 2.1), electrochemical deposition (Figs. 2.2(a) and 2.2(b)) and bacterial colonies (Fig. 2.3). A radial growth problem is convenient to work with as it is fairly simple to handle analytically when using complex analysis. Therefore, such problems have been studied thoroughly for several years. Some well established growth models are presented, together with a derivation of a well known problem using a less established approach.

7.1 Continuous Laplacian growth

The first model considers Laplacian growth of a nearly circular domain in the absence of surface tension. If a perfectly circular domain is growing in a harmonic field U with an equally large gradient at all points of the domain boundary, then the boundary will grow equally fast at all points and hence the circular shape will be preserved. This is not a very relevant example to study because nature itself never provides anything that is perfectly circular. A seemingly circular inlet in viscous fingering will, in practice, provide an initial influx which is not exactly the same in all

directions. This leads to a starting configuration for the pattern evolution which is only nearly circular. A seed particle in solidification experiments will always have some irregularities in the packing at molecular levels, leading to tiny bumps on the surface. What is interesting to know is which effects such irregularities in the initial configuration will have on the final shape.

The model considers a nearly circular domain; more precisely, the unit circle which is perturbed by a function $h(\theta) = \epsilon \cos(m\theta)$, introducing m protruberances of amplitude ϵ around the rim of the unit disc. This is exactly the same starting configuration as for the Mullins-Sekerka stability analysis in Sec. 6.1. The question is how the boundary of this nearly circular domain will evolve in time when it is growing in a Laplacian field U. For simplicity, surface tension is not included in the model. This gives the conformally invariant boundary condition $U(z_b) = 0$ at the points z_b of the boundary of the growing domain, which allows for the use of conformal mapping techniques. Eq. (6.8) for the growth rate of the amplitude ϵ predicts that the perturbation will be unstable when $\Upsilon_C \propto \Upsilon = 0$.

The basic idea behind the use of conformal maps in the study of boundary evolution was presented in Sec. 4.5. In this example, the exterior of the unit circle is a suitable reference domain. The evolution of the boundary is dependent on the Laplacian field between the boundary and infinity, hence this will be the region in which the Laplace equation needs to be solved. In Appendix A, a conformal map $z = f(\omega) = \omega + \epsilon\omega^{-m+1}$ (Eq. (A.17)) from the complement of the unit disc onto the exterior of a slightly distorted unit circle is derived. In order to study the evolution of the boundary $r(\theta) = 1 + h(\theta)$ of the perturbed domain with respect to the unit circle, a dynamical equation for the map $f(\omega)$ is needed. Time dependency in the mapping is introduced by the parameters $\alpha(t)$ and $\beta(t)$, such that

$$f(\omega, t) = \alpha(t)\omega + \beta(t)\omega^{-m+1}. \tag{7.1}$$

The initial conditions $\alpha(0) = 1$ and $\beta(0) = \epsilon$ ensure that $f(\omega, 0) =$

$\omega + \epsilon\omega^{-m+1}$, consistent with Eq. (A.17)

Every harmonic function $U(z)$ can be written as the real part of an analytic function: $U(z) = \mathtt{Re}\ \mathcal{V}(z)$, where $\mathcal{V}(x+iy) = U(x,y) + iW(x,y)$ is called the complex potential. Since $\mathcal{V}(z)$ is analytic, it must satisfy $\frac{\partial \mathcal{V}}{\partial x} = \frac{\partial \mathcal{V}}{\partial (iy)}$, which leads to the Cauchy-Riemann equations:

$$\frac{\partial U}{\partial x} = \frac{\partial W}{\partial y} \tag{7.2}$$

$$\frac{\partial W}{\partial x} = -\frac{\partial U}{\partial y}. \tag{7.3}$$

This can be used to relate the complex potential to the field gradient in Eq. (5.10):

$$\nabla_z U(z) = \frac{\partial U}{\partial x} + i\frac{\partial U}{\partial y} = \frac{\partial U}{\partial x} - i\frac{\partial W}{\partial x} = \left(\frac{\partial \mathcal{V}}{\partial x}\right)^* = \left(\frac{\partial \mathcal{V}}{\partial z}\right)^*, \tag{7.4}$$

in which the asterisk denotes the complex conjugate.

In the exterior of the unit circle, the complex potential will be on the form $\mathcal{V}(\omega) = \log(\omega)$, which will read $\mathcal{V}(z) = \log(f^{-1}(z,t))$ in the z-plane. The normal boundary velocity V_n in the z-plane may then be related to the mapping $f(\omega,t)$ through Darcy's law and Eq. (7.4). Using the exponent $\eta = 1$, the result is

$$V_n \sim \left(\frac{\partial \mathcal{V}}{\partial z}\right)^* = \frac{1}{\omega^* f'(\omega,t)^*}, \tag{7.5}$$

where $f'(\omega,t) = \frac{\partial f}{\partial \omega}$. Another expression for the normal velocity of the surface is found from the time derivative of the mapping $z = f(\omega,t)$:

$$V_n = \frac{d}{dt} f(\omega,t) = \frac{\partial f}{\partial t} + \frac{\partial f}{\partial \omega}\frac{\partial \omega}{\partial \theta}\frac{\partial \theta}{\partial t}.$$

These two equations for V_n together give the dynamical equation for the map:

$$\omega^* \frac{\partial f}{\partial \omega}^* \frac{\partial f}{\partial t} + i\left|\omega \frac{\partial f}{\partial \omega}\right|^2 \frac{\partial \theta}{\partial t} = 1;$$

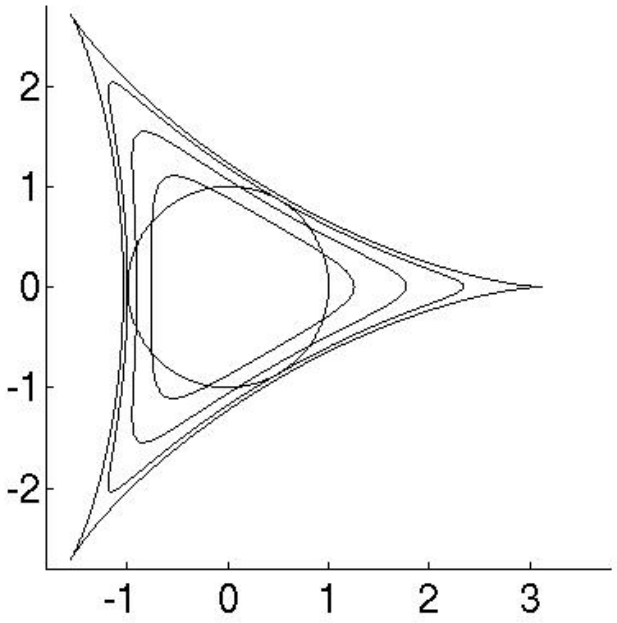

Figure 7.1: The evolution of finite-time singularities from the unit circle, obtained by numerical integration of the Eqs. (7.7) and (7.8), for $m = 3$ and initial conditions $\alpha(0) = 1$ and $\beta(0) = 0.24$.

$$\mathrm{Re}\left(\omega^* \frac{\partial f}{\partial \omega}^* \frac{\partial f}{\partial t}\right) = 1. \tag{7.6}$$

By inserting Eq. (7.1) in Eq. (7.6), a set of differential equations for $\alpha(t)$ and $\beta(t)$ are found:

$$\frac{d\alpha}{dt} = \frac{\alpha(t)}{\alpha^2(t) - (m-1)^2\beta^2(t)} \tag{7.7}$$

$$\frac{d\beta}{dt} = \frac{(m-1)\beta(t)}{\alpha^2(t) - (m-1)^2\beta^2(t)}. \tag{7.8}$$

The set is solved by numerical integration, and the evolution of the boundary is illustrated in Fig. 7.1.

7.2 Pole dynamics

Shraiman and Bensimon showed that the solutions of Eq. (7.6) develop singularities in finite time [Shraiman and Bensimon, 1984]. Due to the relation $V_n = \frac{1}{\omega^* f'(\omega,t)^*}$, there will be a singularity whenever the derivative

$f'(\omega,t)^*$ is zero. As explained in Sec. 4.1, the derivatives of $f(\omega,t)$ can never be zero within the domain in which it is conformal. In this example $f(\omega,t)$ is conformal in the complement of the unit disc, which means that the singularities or poles must lie inside the unit circle.

If $f(\omega,t)$ has the form of Eq. (7.1), its derivative will be an mth order polynomial, and the expression $V_n = \frac{1}{|\alpha(t)+(1-m)\beta(t)\omega^{-m}|}$ has m singularities. These singularities correspond to the number of cusps that are formed on the growing surface. The dynamical equation (7.6) codes not only for the evolution of the perturbed unit circle, but also for the dynamics of the poles lying inside it. This is visualised in Fig. 7.2.

The positions of the poles are given by $\omega = r_m e^{i\theta_m} = \left(\frac{\alpha(t)}{(m-1)\beta(t)}\right)^{\frac{1}{m}}$: the distance r_m from the origin will change, but the angle θ_m with respect to the positive real axis remains the same. These θ_m correspond to the angles at which the surface has the highest normal growth velocity. The interface is moving away from the origin, and so are the poles. At the instant when $\left|\left(\frac{\alpha(t)}{(m-1)\beta(t)}\right)^{\frac{1}{m}}\right| = 1$, the poles hit the rim of the unit disc and enter the domain in which $f(\omega,t)$ is analytic. As a consequence, the cusps on the growing surface develop sharp tips. If the growth is continued, the tips will twist and the mapping loses its invertibility. The cusps are a type of Mullins-Sekerka instability that arise because surface tension is not included in the model. Under these circumstances, there is no force stabilising the infinitely large growth velocities at the thin tips.

7.3 Diffusion-Limited Aggregation

Diffusion-Limited Aggregation (DLA) was first introduced by Witten and Sander in 1981 as a model for random, irreversible aggregation [Witten and Sander, 1981]. It was a discrete version of the dendritic growth models that were already known. It soon turned out that the concept of DLA has applications spanning far away from what was originally intended (see e.g. [Halsey, 2000]).

The model tries to visualise particles that are moving randomly in a

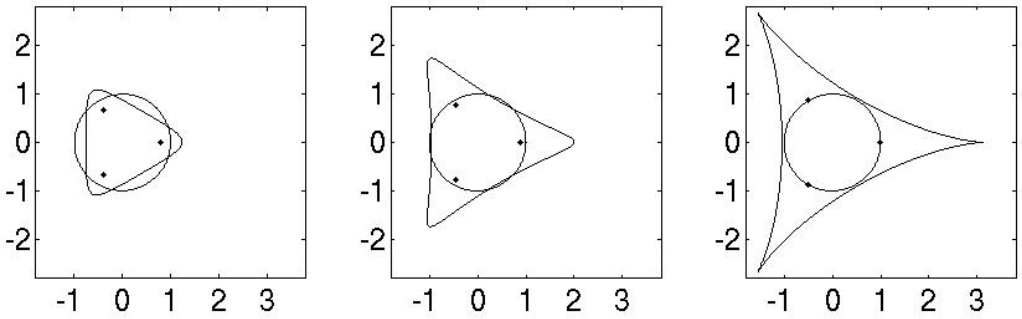

Figure 7.2: An illustration of the pole dynamics for the moving interface obtained from the set of Eqs. (7.21) and (7.22) (to be derived in Sec. 7.6) for $m = 3$. As the surface grows, the poles move away from the origin in the radial direction. The cusps develop sharp tips as the poles hit the rim of the unit circle.

liquid due to Brownian motion. Upon collision, the particles will stick to each other irreversibly, leading to (a) growing cluster(s). An important detail of the model is that the density of particles is low, such that one can assume that only one collision happens at the same instant. This process can be modeled by placing a fixed seed particle in the middle of a lattice, and then releasing a randomly walking particle from somewhere far away from this position. The random walker will either escape to infinity or hit the seed particle. In the case of collision, the random walker will stick to the seed particle and become a part of the cluster. As soon as the first walking particle is out of the game, a second one is released, following the same procedure. This algorithm leads to highly branched clusters with fractal structure. The fractal property arises because the tips shield the other parts of the cluster from incoming particles, and are therefore hit more often and hence grow faster than the inner parts of the stucture.

One example of a structure obtained using this algorithm is presented in Fig. 7.3, which shows clear similarities to the Saffman-Taylor fingering pattern in Fig. 6.2. The Saffman-Taylor problem is an example of a Laplacian growth model. Indeed, this model and DLA have quite similar mathematical descriptions: Saffman-Taylor fingering is controlled by a pressure field that satisfies the Laplace equation, and which is constant at

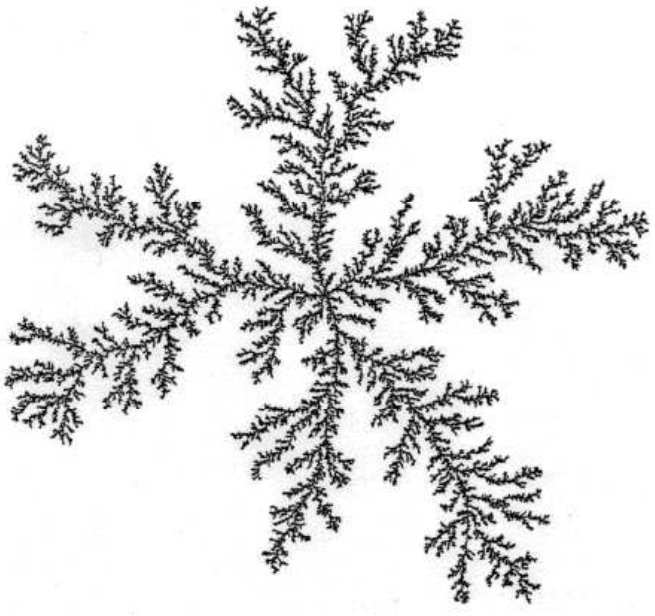

Figure 7.3: The figure shows an example of Diffusion-Limited Aggregation, which is a discrete, stochastic model for colloidal aggregation. The pattern shows similarities to the structure obtained by viscous fingering in Fig 2.1 (from http://classes.yale.edu/ by Michael Frame and Benoit B. Mandelbrot)

the boundary between the two liquids. The interface moves at a velocity proportional to the pressure gradient. In DLA the probability density of random walkers satisfies the Laplace equation, with constant probability density at the surface of the cluster. Here, the probability of growth at the boundary is proportional to the gradient of the probability density. Therefore, DLA can be thought of as the discrete, stochastic analogue of Saffman-Taylor fingering.

The main difference between these two models is that Laplacian growth without surface tension is ill-posed, as was already seen in Sec. 7.1 and Fig. 7.1: the interface is unstable and evolves into singular cusps within finite time. Surface tension or some other regularising effect needs to be intruduced in order to control the singularities and keep the boundary stable. In DLA, these singularity effects are avoided because the particles that are added to the cluster in every growth step have finite size, which acts as a regularisation.

7.4 Iterated maps

Hastings and Levitov showed that iterated conformal maps can be used to study Laplacian growth [Hastings and Levitov, 1998]. After they introduced the idea, it has been applied to many different kinds of growth processes, turning out to be a useful tool. In Sec. 7.1 continuous Laplacian growth governed by Eq. (7.6) was considered. This section concentrates on how to model the same growth discretely. Iterated maps are also often used to produce DLA clusters.

Imagine a structure in physical space that has evolved from a seed particle in discrete growth steps. The goal is to follow the evolution of the mapping $f_n(\omega)$, that maps the exterior of the unit circle in the mathematical ω-plane onto the complement of this structure in the physical z-plane after n growth steps. In order to construct $f_n(\omega)$, the elementary mapping $\varphi_{\lambda_n,\theta_n}(\omega)$ is introduced. This mapping adds a small bump of linear size $\sqrt{\lambda_n}$ to the unit circle, at the angle θ_n around the rim (see Fig. 7.4).

Assume now that the shape of the structure after n growth steps is known and that one wants to find out how it will look after the next step. If the structure is very complex, such as the DLA pattern in Fig. 7.3, then the mapping directly from one growth step to the next in the z-plane will be extremely complicated, even if the changes are very small. A simpler procedure is to make use of the elementary mappings $\varphi_{\lambda_n,\theta_n}(\omega)$ in the mathematical plane. This only requires the knowledge of one single mapping $f_n(\omega)$, which may then be used to study the further growth: if $f_n(\omega)$ maps the unit circle onto the nth step structure in the z-plane, then $f_n(\varphi_{\lambda_{n+1},\theta_{n+1}}(\omega))$ maps the unit circle with a bump onto the $(n+1)$th step structure. The image of $f_n(\varphi_{\lambda_{n+1},\theta_{n+1}}(\omega))$ is the nth step structure with a bump added. The procedure is illustrated in Fig. 7.4. This way the elementary maps can be used to impose controlled changes and growth to the structure in the z-plane, without the hassle of computing new complicated mappings every time the structure changes.

The function $f_n(\omega)$ is practically a composition of n elementary

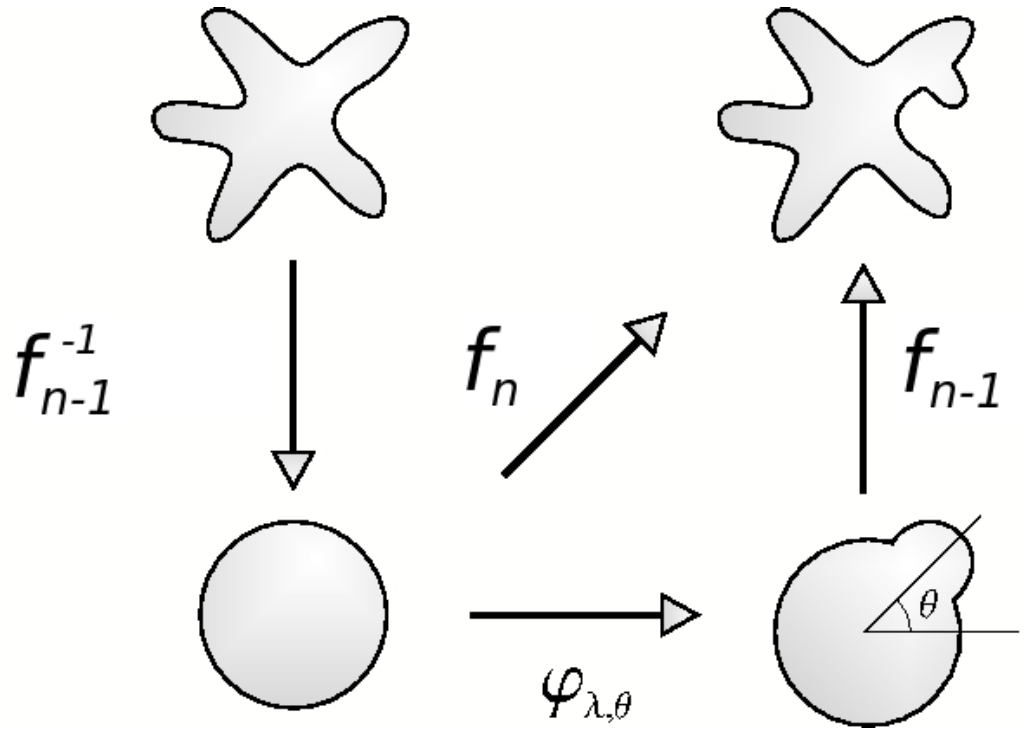

Figure 7.4: The figure illustrates the iterated mapping technique. Mapping directly from one growth step to the next in the physical plane (between the two clusters on the top) gives very complicated expressions as the structure grows and attains a complex shape. A simpler method is to use the mapping $f_{n-1}(\omega)$ between the structure in physical space and the unit circle in the mathematical representation (bottom). The bump map $\varphi_{\lambda,\theta}$ adds a semicircular bump of linear size λ to the unit circle at the angle θ. After adding the bump, this nearly circular boundary can be mapped back to the physical space by $z = f_{n-1}(\varphi_{\lambda,\theta}(\omega))$. This adds a bump to the structure in the z-plane, which is a simple and convenient way to represent growth in the physical plane. Courtesy of Joachim Mathiesen.

mappings $\varphi_{\lambda_n,\theta_n}$:

$$f_n(\omega) = f_{n-1}(\varphi_{\lambda_n,\theta_n}(\omega)). \tag{7.9}$$

A recursive relation that can be used to construct $f_n(\omega)$ reads

$$f_n(\omega) = \varphi_{\lambda_1,\theta_1} \circ \varphi_{\lambda_2,\theta_2} \circ \cdots \circ \varphi_{\lambda_n,\theta_n}(\omega). \tag{7.10}$$

From this it may be concluded that the knowledge of a possibly complicated $f_n(\omega)$ as a starting point for the iteration is never necessary. If desired, the decomposition into elementary mappings can be brought all the way back to $n = 1$, and then letting the initial condition $f_1(\omega)$ be very simple.

The exact way of applying the iterated mapping technique will vary for different growth processes [Barra et al., 2001a]. For DLA, λ_n has to be chosen in such a way that all the particles added in the z-plane are of the same size. The particles are added to the physical boundary with random probability according to the harmonic measure. The probability for a particle to hit the boundary at a certain point is proportional to the gradient of the probability field locally at that point, which again is dependent on the surface shape: the tips are more likely to be hit than the inner parts of the fjords. The harmonic measure is uniform around the unit circle $e^{i\theta}$ in the ω-plane, such that the probability $P(\theta)d\theta = \frac{d\theta}{2\pi}$ for a particle to hit a part $d\theta$ of the unit circle is everywhere the same. With s an arc-length parameterisation of the boundary of the cluster, the uniform measure $P(\theta)$ can be translated to the measure $P(s)$ in the z-plane, using the mapping $z(s) = f_n(e^{i\theta})$. In Sec. 7.1 the complex potential for radial growth was found to be $\mathcal{V}(z) = \log f_n^{-1}(z)$. The harmonic measure in the z-plane then reads

$$P(s)ds \sim |\nabla \mathcal{V}(s)|ds = \frac{1}{|f_n'|}ds$$

[Jensen et al., 2002], [Davidovitch et al., 1999], which in other words expresses the probability that a particle will hit the boundary along an arc ds centered at $z(s)$.

In Laplacian growth, a layer rather than a single particle is added in every iteration. A layer can be represented by j nonoverlapping bumps that are added simultaneously at the positions $\{\theta_i\}_{i=1}^{j}$. The boundary is divided into j segments and in every iteration a bump of linear size proportional to the local value of $|\nabla U|$ is added to each of them. Using this kind of growth regime, f_n needs to be updated every time a whole layer consisting of j bumps has been added to the structure. Using a composition of j different maps $\varphi_{\lambda_{n+i},\theta_{n+i}}$, this can be done with the formula

$$f_{n+j}(\omega) = f_n \circ \varphi_{\lambda_{n+1},\theta_{n+1}x} \circ \cdots \circ \varphi_{\lambda_{n+j},\theta_{n+j}}(\omega)$$

[Barra et al., 2001b]. The procedure is illustrated in Fig. 7.5.

The choice of $\{\lambda_{n+i}\}_{i=1}^{j}$ and $\{\theta_{n+i}\}_{i=1}^{j}$ is not trivial in this case; each λ_{n+i} is proportional to the local field, which again depends on the shape of the surface at the corresponding position θ_{n+i}. Fig. 7.5 illustrates how the bumps that are added at protuberances on the surface are larger than the ones added at depressions. The tips are more available to incoming flux of e.g. heat or mass, and thus tend to grow faster than the more screened parts of the surface. The field gradient is therefore much larger around a sharp tip than at a flat surface, and hence the bump size λ_i must also follow this rule. Simultaneously, $\{\theta_i\}_{i=1}^{j}$ is no longer uniformly distributed on the unit circle, as was the case for DLA, because one must avoid overlaps. When a new layer of particles has been added, the new shape of the cluster leads to a change in the field such that the mapping needs to be updated. This involves a reparameterization of the unit circle, which means that $\{\theta_{n+i}\}_{i=1}^{j}$ must also be updated each time a new layer of particels is added. The effect of this reparameterisation is to make sure that there is a correct relationship between the sizes and positions of the j particles that are added in the next layer. Without this, the changing shape of the surface could eventually lead to the gradual displacement of the particles in each growth step, such that after a while small particles end up at the tips whereas larger ones are added in fjords.

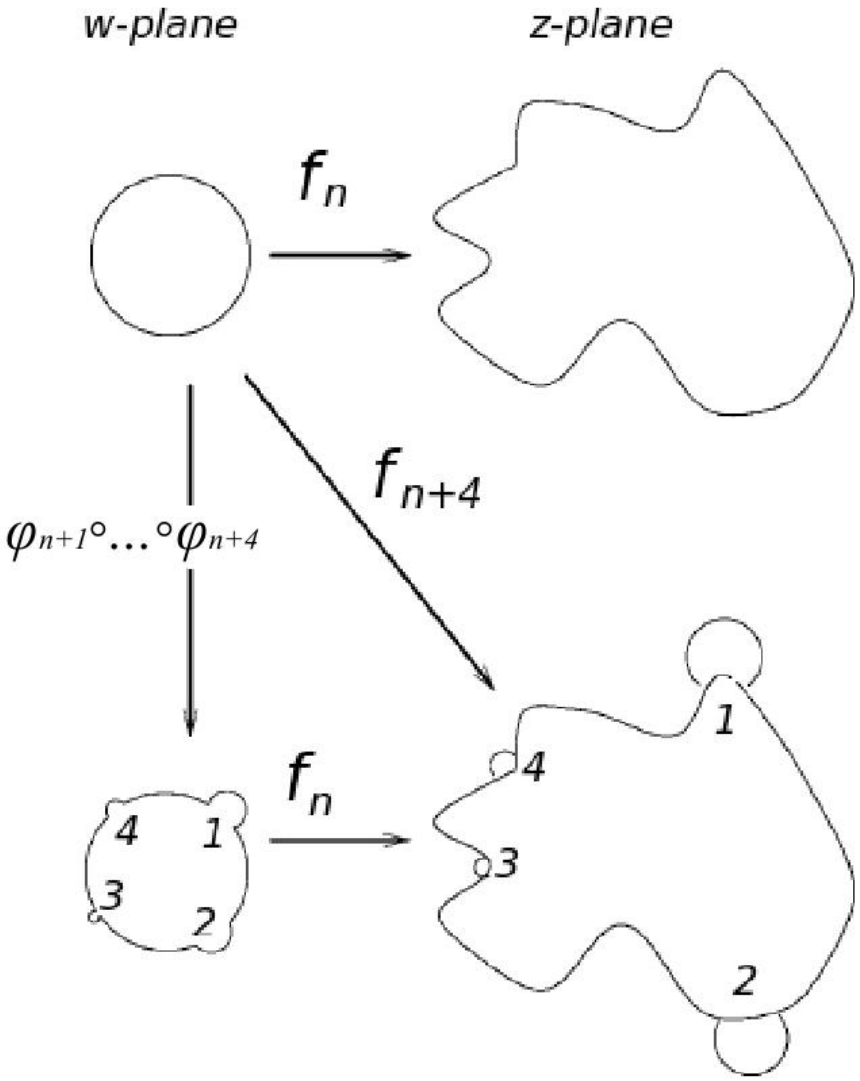

Figure 7.5: An illustration of how iterated maps can be used to represent Laplacian growth. In this situation a layer rather than a single particle is to be added to the boundary in each growth step, which can be done by adding several nonoverlapping bumps. A certain number of bumps are added to the unit circle in each iteration, before mapping back to the z-plane. The figure is modified from [Barra et al., 2001b].

7.5 Conformal radius and fractal dimension

The conformal map $f(\omega)$ is analytic in the exterior of the unit circle, which allows it to be represented by a Laurent series: $f(\omega) = ...F_2\omega^2 + F_1\omega + F_0 + F_{-1}\omega^{-1} + F_{-2}\omega^{-2} + ...$ By the Riemann mapping theorem, f is the unique mapping of the exterior of the unit circle onto the complement of some simply-connected domain D. It must therefore be linear in ω when $\omega \to \infty$, and hence the coefficients of the second and higher order terms in the expansion must be zero. F_1 must be nonzero, due to the fact that the mapping is conformal at infinity and thus needs a nonzero derivative there. The expansion can therefore be written as

$$f(\omega) = F_1\omega + F_0 + F_{-1}\omega^{-1} + \dots \tag{7.11}$$

$f(\omega)$ maps ∞ to ∞, which requires that $F_1 > 0$. F_1 is called the conformal radius of D, and F_0 is its conformal center.

There are a number of theorems regarding the Laurent coefficients of univalent functions, among them is the Koebe one-quarter theorem. If the unit circle is mapped to the z-plane by a function of the form of Eq. (7.11), the image will be a closed curve: more precisely it will be the boundary of the domain D. The Koebe theorem can be used to show that this curve must be contained within a circle of radius $4F_1$. Hence the first order coefficient of the Laurent expansion of the conformal map will scale as the size of the cluster which is the image of the mapping. This can be used to obtain an estimate of the fractal dimension $\mathscr{D}_F$ of the cluster, by comparing the area $\mathscr{A}$ of the cluster to its maximum radius: $\mathscr{A} \sim (4F_1)^{\mathscr{D}_F}$.

The area theorem is another rule for univalent functions. It states that if the exterior of the unit circle is mapped to the exterior of a simply-connected domain D by a function of the form of Eq. (7.11), then the area of D is related to the Laurent coefficients of the mapping by

$$\mathscr{A} = |F_1|^2 - \sum_{j=1}^{\infty} j|F_{-j}|^2.$$

If the growing structure is the image of a mapping of the form of Eq. (7.1), this may be a useful way of estimating its area and hence its fractal dimension. If the structure is the result of an iteration of many elementary maps, such as the mapping in Eq. (7.10), its area may be found from easier considerations. Recall that the elementary map $\varphi_{\lambda_n,\theta_n}$ adds a bump of linear size $\sqrt{\lambda_n}$ to the cluster. The unit circle is then mapped onto the boundary of a cluster of n particles of roughly the same linear size $\sqrt{\lambda_0}$. The area $\mathscr{A}_n$ of this cluster is therefore approximated by $\mathscr{A}_n \sim n\lambda_0$.

7.6 Iterated maps in the continuous limit

Both continuous and discrete Laplacian growth has been presented in this chapter. The continuous case is based on a dynamical equation derived from Darcy's law and the time derivative of the mapping of the surface. The discrete version considers iterated conformal maps. This section introduces a new approach to the well known problem: the derivation of continuous time dependency of the parameters of the mapping, using some of the ideas from iterated conformal maps.

Start once again from Eq. (A.17), $z = f(\omega) = \omega + \epsilon\omega^{-m+1}$, which maps the unit circle $\omega = e^{i\theta}$ onto the structure in the z-plane. In Sec. 7.4 it was stated that Laplacian growth can be modeled by adding a thin layer to the boundary of the structure in each iteration step. It was explained how the use of bump maps $\varphi_{\lambda,\theta}(\omega)$ to add this layer gets quite complicated because of the nontriviality that lies in picking the correct parameters λ and θ in each step. The derivation in this section is based on the idea that the whole layer can be added in one single iteration: the mapping $\varphi(\omega)$ adds a thin layer to the unit disc ω through

$$\varphi(\omega) = |\omega| + |d\omega|. \tag{7.12}$$

In other words, the boundary ω of the unit disc is now time dependent: $\omega = \omega(t)$. The changes that this introduces in the mathematical plane is what makes the structure in the z-plane change, through $f(\omega(t)) =$

$\omega(t) + \epsilon\omega(t)^{-m+1}$.

The normal velocity V_n of the boundary of the structure in the z-plane is

$$V_n = \frac{dz}{dt} = \frac{df(\omega)}{d\omega}\frac{d\omega}{dt} = f'(\omega)\frac{d\omega}{dt}.$$

Combined with Eq. (7.5) found from Darcy's law in Sec. 7.1, this gives the expression

$$\frac{d\omega}{dt} = \frac{1}{\omega^* f'(\omega)^* f'(\omega)} = \frac{\omega}{|f'(\omega)|^2}$$

for how ω chages in time. This can be used to rewrite Eq. (7.12) into

$$\varphi(\omega) = |\omega| + \Big|\frac{\omega\, dt}{|f'(\omega)|^2}\Big| = 1 + \frac{dt}{|f'(\omega)|^2}.$$

Now $\varphi(\omega)$ is just another way of representing the nearly circular domain with boundary $r(\theta) = 1 + h(\theta)$, which is discussed in Sec. 7.1 and in Appendix A. Appendix A contains a derivation of an equation for a mapping from the unit circle onto such a perturbed domain (Eq. (A.16)). With $|d\omega| = h(\theta) = \frac{dt}{|f'(\omega)|^2}$, this equation now reads

$$\varphi(\omega) = \omega + \frac{\omega}{2\pi}\int_0^{2\pi} \frac{e^{-i\phi} + \omega}{e^{-i\phi} - \omega}\frac{dt}{|f'(e^{-i\phi})|^2}\, d\phi. \tag{7.13}$$

As long as $|d\omega|$ is small, the expansion $f(\varphi(\omega)) \approx f(\omega) + \frac{df}{d\omega}[\varphi(\omega) - \omega]$ can be made. In combination with Eq. (7.13), the change of $f(\omega)$ in time is found from

$$\frac{f(\varphi(\omega)) - f(\omega)}{dt} = \frac{d}{dt}f(\omega) = \frac{df(\omega)}{d\omega}\frac{\omega}{2\pi}\int_0^{2\pi} \frac{e^{-i\phi} + \omega}{e^{-i\phi} - \omega}\frac{1}{|f'(e^{-i\phi})|^2}\, d\phi.$$

It is about time to transfer the time dependency from $\omega(t)$ and into the function $f(\omega)$ itself. This is done by replacing $f(\omega)$ by Eq. (7.1), exactly as in Sec. 7.1. $f(\omega(t))$ is not linear in $\omega(t)$, but as the mapping is applied repeatedly, the time parameter can be withdrawn from $\omega(t)$ and put into the parameters $\alpha(t)$ and $\beta(t)$ in Eq. (7.1).

The equation of motion for the growing interface in the z-plane now

reads

$$\frac{\partial f(\omega,t)}{\partial t} = \frac{\partial f(\omega,t)}{\partial \omega}\frac{\omega}{2\pi}\int_0^{2\pi}\frac{e^{-i\phi}+\omega}{e^{-i\phi}-\omega}\frac{dt}{|f'(e^{-i\phi},t)|^2}\,d\phi. \tag{7.14}$$

Eq. (7.14) is now used to derive a set of differential equations for $\alpha(t)$ and $\beta(t)$:

$$\frac{d\alpha}{dt}\omega + \frac{d\beta}{dt}\omega^{-m+1} = \left(\alpha(t) + (1-m)\beta(t)\omega^{-m}\right)$$

$$\cdot\frac{\omega}{2\pi}\int_0^{2\pi}\frac{e^{-i\phi}+\omega}{e^{-i\phi}-\omega}\frac{d\phi}{\left[\alpha(t)+(1-m)\beta(t)e^{-im\phi}\right]\left[\alpha(t)+(1-m)\beta(t)e^{im\phi}\right]}.$$

Introduce the abbreviation $I(\omega) = \varphi(\omega) - \omega$, and let $k_1 = \alpha^2(t) + (1-m)^2\beta^2(t)$, $k_2 = \frac{\alpha(t)(1-m)\beta(t)}{k_1}$ and $\tilde{\omega} = e^{i\phi}$; then

$$I(\omega) = \frac{\omega}{2\pi k_1}\int_0^{2\pi}\frac{\tilde{\omega}^{-1}+\omega}{\tilde{\omega}^{-1}-\omega}\frac{1}{\left[1+k_2(\tilde{\omega}^m+\tilde{\omega}^{-m})\right]}\frac{d\tilde{\omega}}{i\tilde{\omega}}. \tag{7.15}$$

The polynomial in the denominator can be rewritten as $\tilde{\omega}^m + k_2\tilde{\omega}^{2m} + k_2 = (\tilde{\omega}^m - c_1)(\tilde{\omega}^m - c_2)$, where $c_1 = -\frac{1}{2k_2} - \sqrt{\frac{1}{4k_2^2}-1}$ and $c_2 = -\frac{1}{2k_2} + \sqrt{\frac{1}{4k_2^2}-1}$. The integral then reads

$$I(\omega) = \frac{\omega}{2\pi i k_1}\int_0^{2\pi}\frac{\tilde{\omega}^{-1}+\omega}{\tilde{\omega}^{-1}-\omega}\frac{\tilde{\omega}^m}{(\tilde{\omega}^m-c_1)(\tilde{\omega}^m-c_2)}\frac{d\tilde{\omega}}{\tilde{\omega}}.$$

The product of the two poles of the general quadratic equation $Ax^2 + Bx + C$ is $\frac{-B+\sqrt{B^2-4AC}}{2A}\frac{-B-\sqrt{B^2-4AC}}{2A} = \frac{C}{A}$. In this example this means that the product $c_1c_2 = 1$, from which it can be concluded that one of the roots c_1 or c_2 lies inside the unit circle, and the other one outside. Since k_2 is a small, positive number, c_2 must lie closer to the origin than c_1. Therefore, only c_1 lies inside the integration area.

The exact solution of $I(\omega)$ is a sum of the residues of the (m+1) poles

within the integration area:

$$I(\omega) = \frac{-2\omega^{-m+1}}{k_1(\omega^{-m}-c_1)(\omega^{-m}-c_2)} \tag{7.16}$$
$$+\frac{\omega}{k_1(c_1-c_2)}\sum_{j=0}^{m-1}\frac{e^{\frac{-2\pi ij}{m}}+\omega c_1^{\frac{1}{m}}}{\left(1-\omega c_1^{\frac{1}{m}}e^{\frac{2\pi ij}{m}}\right)\prod_{n=0}^{j-1}\left(e^{\frac{2\pi ij}{m}}-e^{\frac{2\pi in}{m}}\right)\prod_{n=j+1}^{m-1}\left(e^{\frac{2\pi ij}{m}}-e^{\frac{2\pi in}{m}}\right)}.$$

Obviously, the exact solution does not straight-forwardly lead to expressions for $\alpha(t)$ and $\beta(t)$. As a simplification, the special case $m = 3$ can be considered, such that the result can be compared to what was obtained in Sec. 7.1 and by [Barra et al., 2001b]. Computing the sum for $m = 3$ gives the expression

$$I_{m=3}(\omega) = \frac{-2\omega^{-2}}{k_1(\omega^{-3}-c_1)(\omega^{-3}-c_2)} - \frac{\omega}{2k_1\sqrt{\frac{1}{4k_2^2}-1}}\frac{1+\omega^3 c_1}{(1-\omega^3 c_1)}. \tag{7.17}$$

A series expansion around infinity of the product $\frac{\partial f(\omega,t)}{\partial t} I_{m=3}(\omega)$ gives expressions for the modes ω and ω^{-2} which can be put equal to the left-hand side of Eq. (7.14), giving the equation set

$$\frac{d\alpha}{dt} = \frac{\alpha(t)k_2}{k_1\sqrt{1-4k_2^2}} \tag{7.18}$$
$$\frac{d\beta}{dt} = \frac{2k_2}{k_1\sqrt{1-4k_2^2}}\left(\frac{\alpha(t)}{c_1}-\beta(t)\right) - \frac{2\alpha(t)}{k_1} \tag{7.19}$$

The equations cannot be solved analytically. By numerical integration, using the fourth order Runge-Kutta method, the same behaviour as in Fig. 7.1 is obtained.

In order to obtain analytic solutions of $\alpha(t)$ and $\beta(t)$ for any m, the integral in Eq. (7.15) must be simplified. This is done by using the expansion $\frac{1}{1+k_2(\tilde{\omega}^m+\tilde{\omega}^{-m})} \approx 1 - k_2(\tilde{\omega}^m + \tilde{\omega}^{-m})$. The result of the

integration now reads

$$I_{aprx}(\omega) = \frac{1}{k_1}\omega - \frac{2k_2}{k_1}\omega^{-m+1}.$$

Inserting $I_{aprx}(\omega)$ into Eq. (7.14) and collecting powers of ω leads to a new set of differential equations:

$$\begin{aligned} \frac{d\alpha}{dt} &= \frac{\alpha(t)}{k_1} \\ \frac{d\beta}{dt} &= \frac{\beta(t)(1-m)}{k_1} - \frac{2k_2\alpha(t)}{k_1} \\ 2k_2\beta(t)(1-m) &= 0. \end{aligned} \tag{7.20}$$

The derivation is based on a small perturbation amplitude, and therefore it can be assumed that $\beta(t) \ll \alpha(t)$. The simplifitacion of setting all second- and higher order terms of $\beta(t)$ to zero is therefore valid. With $k_1 = \alpha^2(t)$ and $k_2 = \frac{\beta(t)(1-m)}{\alpha(t)}$, the solutions read

$$\alpha(t) = \sqrt{\alpha(0)^2 + 2t} \tag{7.21}$$

$$\beta(t) = \beta(0)\left(\frac{\alpha(t)}{\alpha(0)}\right)^{(m-1)}. \tag{7.22}$$

Once again, the solution reproduces what is seen in Fig. 7.1 for $m = 3$. Eqs. (7.21) - (7.22) are used to produce the pole dynamics plot in Fig. 7.2.

Chapter 8

Loewner evolution

Charles Loewner developed another technique for studying pattern growth by means of conformal maps [Löwner, 1923]. The motivation for his work was the Bieberbach conjecture, which states a necessary condition on a holomorphic function $g(z)$ to injectively map the open unit disc in the complex plane to the entire complex plane. The condition is that the coefficients of the Taylor expansion $g(z) = \sum_{n\geq 2} c_n z^n$ must satisfy $|c_n| \leq n$ for all $n \geq 2$. Loewner developed a differential equation for conformal maps, and used it to prove that $c_3 \leq 3$.

However, the result of Loewner's work has many other applications. In 2001, Carleson and Makarov showed that the Loewner differential equation could be used to study growth and aggregation processes, using DLA and Laplacian growth without surface tension in a Hele-Shaw cell as examples [Carleson and Makarov, 2001]. Later, the method has been applied to many different examples of growth, such as fingered growth in channels, random walks and Brownian motion (see e.g. [Bauer and Bernard, 2006] or [Gubiec and Szymczak, 2008]).

8.1 The Loewner equation

The derivation of the Loewner equation uses compositions of conformal maps, combined with some theories from complex analysis and statistical

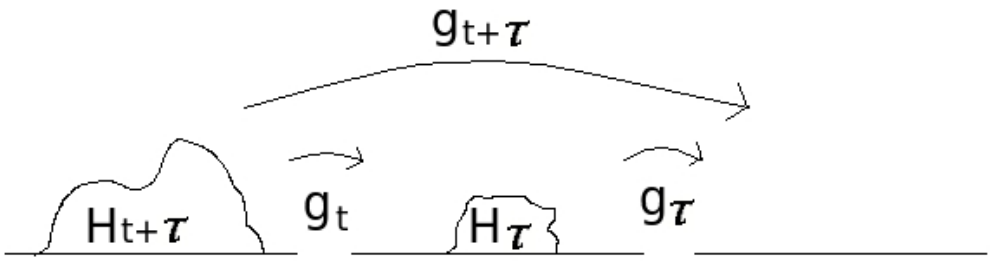

Figure 8.1: Illustration of how the map g_t absorbs the growing structure H_t in successive steps. The mapping $g_{t+\tau}$ is a composition of many small steps g_τ.

physics. Let the upper half-plane be the reference domain R, whereas a shape growing from the real axis and into the upper half-plane in physical space is called H_t. The boundary of H_t and the remainder of the real axis together make up the boundary of a domain D in the z-plane, which is simply the upper half-plane with H_t subtracted: $D = R \backslash H_t$. A conformal transformation $g_t(z)$ maps D onto R, and brings the boundary of D onto the real axis. Here t represents a time parameterization that corresponds to the t in H_t. At time $t + \tau$ an increment H_τ has been added to the shape in the z-plane, such that it has grown into $H_{t+\tau} = H_t + H_\tau$. $H_{t+\tau}$ contains H_t, and the transformation $g_{t+\tau}$ maps the now smaller D onto R. This means that as H_t evolves with time, the mapping $g_t(z)$ must also change in order to at any instant be able to map D onto the reference domain R. Note that the composition property can be very useful when working with this kind of evolution: At time $t + \tau$ the shape $H_{t+\tau}$ can be mapped to the reference domain in two ways: either by $g_{t+\tau}(z)$ or by $g_\tau(g_t(z))$ (see Fig. 8.1). Since $g_{t+\tau}(z) = g_\tau(g_t(z))$ it follows that $g_t(z) = g_\tau^{-1}(g_{t+\tau}(z))$. By letting $\tau \to 0$, this can be used to derive a differential equation for the map $g_t(z)$. One way of presenting this equation is obtained from [Fogedby, 2007]:

$$\frac{dg_t(z)}{dt} = \frac{1}{\pi} \int \frac{\rho_t(\omega)\, d\omega}{g_t(z) - \omega}, \tag{8.1}$$

where $\rho_t(\omega)$ is called the Loewner density and is the parameter that really controls the growth.

Eq. (8.1) can be simplified in the special case where the growth takes place at a single point, which implies that H_t essentially is a curve growing into the upper half-plane. The growth happens at the point $a(t)$ on this curve, and it may be shown that the density $\rho_t(\omega)$ is concentrated in this point, such that $\rho_t(\omega) = 2\pi\delta(\omega - a(t))$[1] . Making this substitution in Eq. (8.1), one lands at the Loewner equation:

$$\frac{dg_t(z)}{dt} = \frac{2}{g_t(z) - a(t)}. \tag{8.2}$$

$a(t)$ is always real valued, and is called the driving function. From its coupling to $\rho_t(\omega)$ it is easy to see that this is the parameter that controls the growth of the curve. The initial condition $g_0(z) = z$ of Eq. (8.2) implies that the z-plane is mapped into itself by $g_t(z)$ when $t = 0$. The boundary condition at infinity is that g_t is the identity map: $g_t(z) = z + o(\frac{1}{z})$ as $z \to \infty$.

Observe that Eq. (8.2) has a singularity when $g_t(z) = a(t)$. The fact that $a(t)$ is real and therefore sits on the boundary of R implies that the critical points $z = g_t^{-1}(a(t)) = \gamma_t$ must belong to the boundary of D. γ_t is the tip of the curve Γ_t that grows into the upper half-plane, and this curve is actually a trace of the singularities of Eq. (8.2). The composition property of conformal maps implies that if a point is in the trace at some time t, then it will remain a part of it for all subsequent times. This means that all growth takes place at the tip of the curve.

A continuous driving function will yield a continuous trace, whereas jumps in the driving function will result in a discontinuous trace. It can be shown that if $a(t)$ is smooth enough, such that it is everywhere differentiable, then the trace never intersects itself. A complex driving function will give a more complex trace Γ_t. The trace can intersect itself if $a(t)$ is sufficiently singular. Moreover, if the driving function is periodic

[1] δ is the Kronecker Delta.

the trace will be a self-similar curve [Gruzberg and Kadanoff, 2004]. Fig. 8.2 shows some examples of traces for different driving functions.

8.2 Example: a growing stick

Consider now the simple example when H_t is a straight line growing into the upper half-plane from the origin, perpendicularly to the real axis. More precisely, it is a curve or trace Γ_t to which a small increment is added at the tip in every time step. This configuration is obtained by using the driving function $a(t) = 0$. Solving Eq. (8.2) then yields the expression

$$g_t(z) = \sqrt{z^2 + 4t}$$

for the map. The inverse $f_t(\omega)$ of $\omega = g_t(z)$ reads $f_t(\omega) = \sqrt{\omega^2 - 4t}$. By inspection of the two maps, it can be concluded that $g_t(z)$ maps the upper half-plane minus a line segment Γ_t from 0 to $2i\sqrt{t}$ onto the entire upper half-plane. The right hand side of the line segment is mapped to the interval from 0 to $2\sqrt{t}$ on the real axis, whereas the left hand side is mapped to the part between $-2\sqrt{t}$ and 0, as illustrated in Fig. 8.3

Using instead a constant $a(t) = c$ when solving Eq. (8.2), the solution

$$g_t(z) = c + \sqrt{(z-c)^2 + 4t} \tag{8.3}$$

is obtained. The growing structure in the z-plane is now a curve from $z = c$ to $z = c + 2i\sqrt{t}$, which is mapped to the segment between $c - 2\sqrt{t}$ and $c + 2\sqrt{t}$ on the real axis in the reference domain by $g_t(z)$.

8.3 Numerical procedure

The numerical method used to find the trace of $\gamma_t = g_t^{-1}(a(t))$ in the Loewner evolution follows the idea of iterated elementary maps. Under time discretisation, the trace will be a set of points, and the curve Γ_t will be the line connecting these points. In the limit of infinitesimally small time

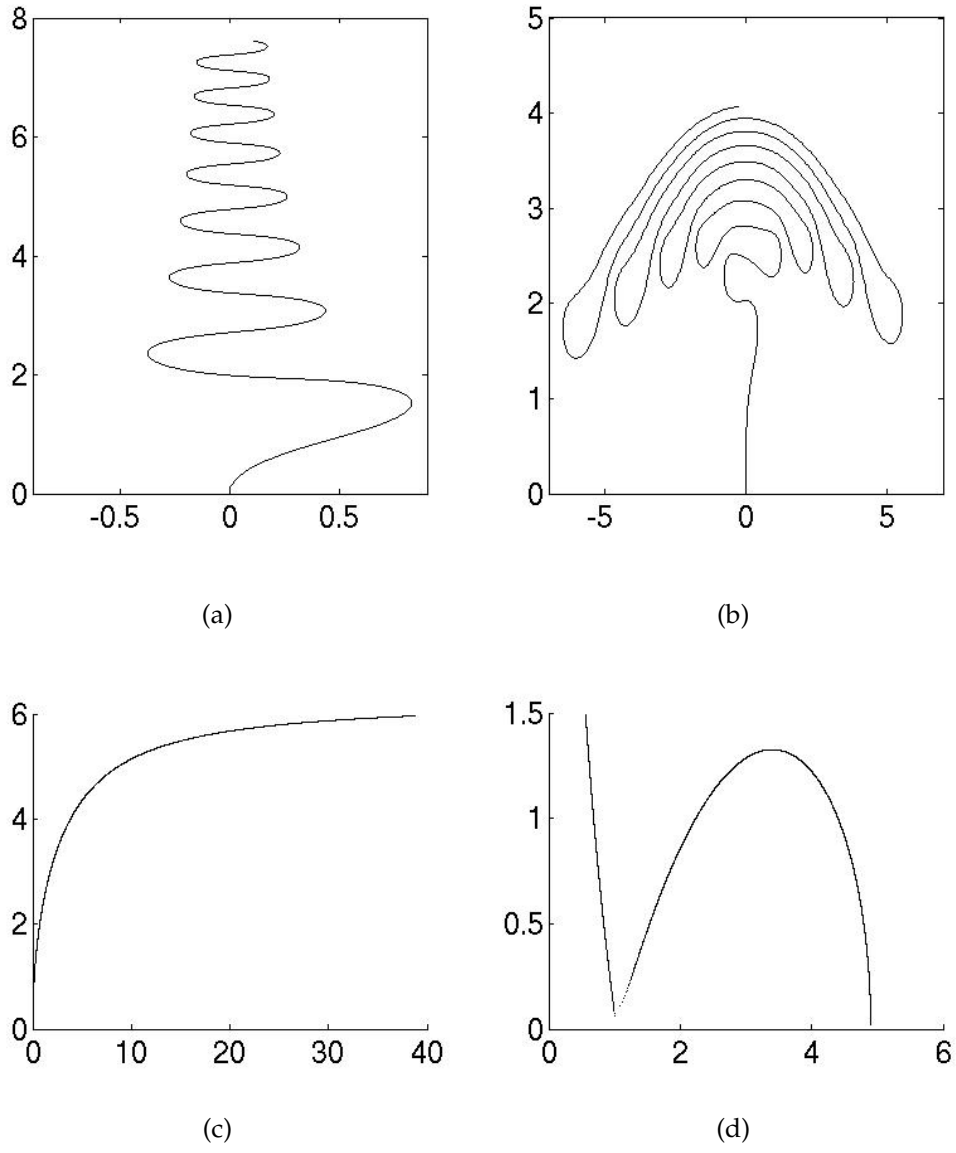

Figure 8.2: Examples of the trace of the Loewner evolution for different driving functions: (a) $a(t) = \sin(\pi t)$, (b) $a(t) = t\sin(\pi t)$, (c) $a(t) = t$, and (d) $a(t) = 2\sqrt{6(1-t)}$ for $t \in (0,1)$ and $a(t) = 0$ for $t \geq 1$. In (d), the trace starts growing from a point close to 5 on the real axis, then grows in an arc to the left until it touches the real axis again when $t = 1$. For $t > 1$, the trace once again grows up into the upper half-plane.

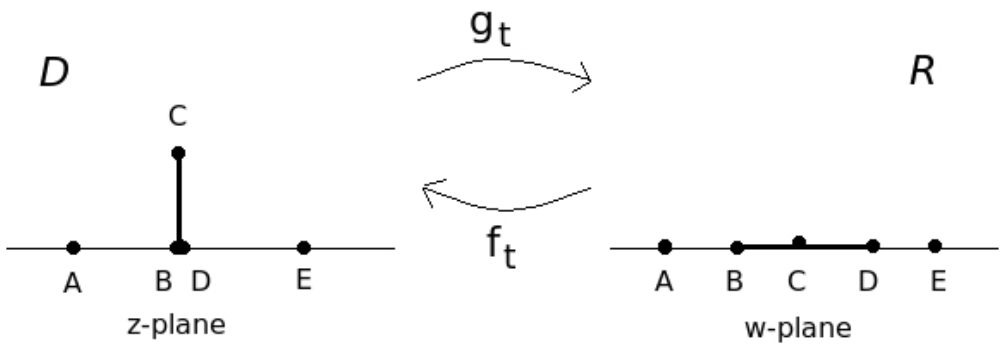

Figure 8.3: A simple example of Loewner evolution: a stick is growing in the z-plane, with the end point C moving further into the upper half-plane with increasing time. At any instant, the corresponding time dependent mapping g_t maps the domain D, which is the upper half-plane minus the growing stick, onto the entire upper half-plane R. The evolution of g_t is coded by the Loewner equation.

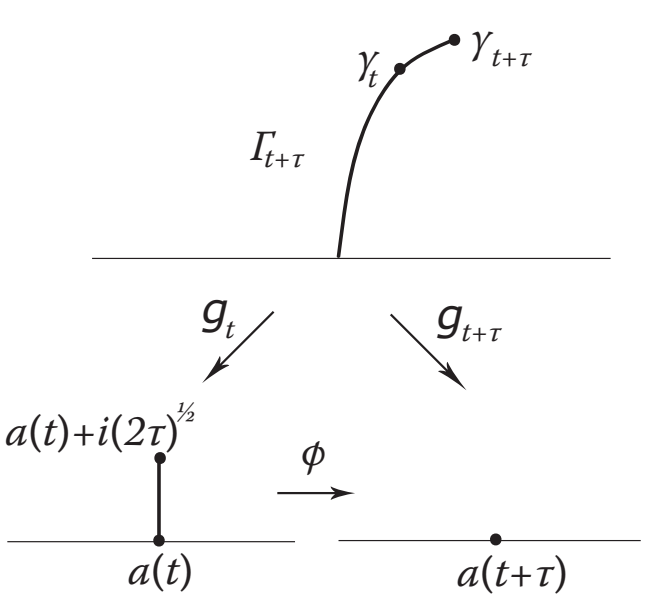

Figure 8.4: An illustration of how the conformal map g_t that satisfies the Loewner equation (8.2) is a composition of elementary slit maps ϕ. A new line segment is added at the tip of the curve Γ_t in each time step τ. γ_t is the tip of Γ_t at time t. The map $g_{t+\tau}$ must consist of the map g_t that takes the old tip γ_t to the real axis, composed with the slit mapping ϕ that maps the line segment from γ_t to $\gamma_{t+\tau}$ to the real axis.

steps τ, Γ_t will be a smooth curve. This leads to the idea that the trace can be drawn as a composition of many short, straight line segments. In each time step, a new line segment is added to the tip of the existing curve Γ_t.

The map g_t is constructed by the composition $g_{t+\tau} = \phi \circ g_t$ where ϕ is the slit mapping

$$\phi(z) = a(t) + \sqrt{(z - a(t))^2 + 4\tau}. \tag{8.4}$$

The slit mapping ϕ is similar to the mapping in Eq. (8.3) and has more or less the same effect: it maps the straight line between the points $a(t)$ and $a(t) + 2i\sqrt{\tau}$ (the slit) onto the real axis, and takes the tip of the slit to the point $a(t + \tau)$. The method is illustrated in Fig. 8.4. The figure shows that g_t will map the tip of the growing curve Γ_t to the point $a(t)$ on the real axis at any time t. When the trace Γ_t grows from time t to $t + \tau$, g_t maps the segment between the real axis and γ_t to the real axis, whereas the slit mapping ϕ takes the part that has been added at the tip, between γ_t and $\gamma_{t+\tau}$, to the real axis.

In most applications of the Loewner equation, one wants to find the trace Γ_t for a given driving function $a(t)$. This means that not g_t, but rather its inverse f_t is of interest. A differential equation for f_t may be derived using the same approach as for g_t. However, both the derivation and the resulting equations will be more complicated than for g_t (Eqs. (8.1) and (8.2)). f_t is instead found by inverting the composition relation $g_{t+\tau} = \phi \circ g_t$, giving

$$f_{t+\tau} = f_t \circ \varphi \tag{8.5}$$

where $\varphi = \phi^{-1} = a(t) + \sqrt{(\omega - a(t))^2 - 4\tau}$.

Eq. (8.5) shows that an explicit knowledge of the mapping f_t itself is never required, because it is a composition of elementary mappings φ with the initial condition $f_0(\omega) = \omega$, such that $f_t(\omega) = \varphi_\tau \circ \varphi_{2\tau} \circ ... \circ \varphi_t(\omega)$. In the limit $\tau \to 0$, the points mapped by the φ's trace out a smooth curve.

The behaviour of the trace is very sensitive to the sign of the term $\omega - a(t)$ in φ. If φ is computed using the equation $\varphi = a(t) + \sqrt{(\omega - a(t))^2 - 4\tau}$, this sign is supressed as the term is raised to the

second power inside the square root. If the equation is rewritten as $\varphi = a(t) + (\omega - a(t))\sqrt{1 - \frac{4\tau}{(\omega - a(t))^2}}$, the correct sign is maintained throughout the iterations. However, when φ is on this form an exception must be included to the algorithm whenever $\omega = a(t)$, to ensure that the imaginary part of φ correctly equals $2\sqrt{\tau}$ when this equality occurs.

8.4 The Loewner equation for radial Laplacian growth

Radial Laplacian growth was studied in Chapter 7, and in Sec. 7.6 the growth process was modeled in discrete time by the addition of a thin layer $|d\omega|$ to the unit disc in every time step. Eq. (7.14) was derived to describe how the mapping of the growing structure would change as an effect of the addition of this layer. This is a differential equation for a conformal map, and as such it represents an example of Loewner evolution. With the time parameterisation notation the equation can be written as

$$\frac{d}{dt} f_t(\omega) = \omega f_t'(\omega) \frac{1}{2\pi i} \oint \frac{\omega + u}{\omega - u} \frac{du}{u|f_t'(u)|^2}. \tag{8.6}$$

The term $\frac{1}{|f_t'(u)|^2}$ was derived from Darcy's law and is the Loewner density $\rho_t(u)$ for radial Laplacian growth.

Loewner evolution may be used to study other types of radial growth aswell. To derive a generalised version of the Loewner equation for radial growth, Eq. (8.6) is rewritten as

$$\frac{\frac{d}{dt} f_t(\omega)}{\omega f_t'(\omega)} = \frac{1}{2\pi i} \oint \frac{\omega + u}{\omega - u} \frac{\rho_t(u)}{u} \, du. \tag{8.7}$$

Observe that this equation can be regarded as the solution of a boundary value problem on the unit circle: $\frac{\frac{d}{dt} f_t(\omega)}{\omega f_t'(\omega)}$ is the function which is analytic in the exterior of the unit circle, and whose real part on the unit circle is $\mathrm{Re}\left\{ \frac{\frac{d}{dt} f_t(\omega)}{\omega f_t'(\omega)} \right\} = \rho_t(u)$.

$f_t(\omega)$ maps the unit circle onto the boundary of the growing domain. The normal velocity of this boundary can be expressed as

$$V_n = |f_t'(\omega)| \ \mathtt{Re} \ \left\{ \frac{\frac{d}{dt} f_t(\omega)}{\omega f_t'(\omega)} \right\} \tag{8.8}$$

[Bauer and Bernard, 2006]. As long as the boundary velocity in a growth process is known, it can be linked to the Loewner density by Eq. (8.8). This admits the growth problem to be solved using the Loewner equation for radial growth processes, Eq. (8.7).

Chapter 9

Fingered growth

Surface instabilities can lead to the formation of fingerlike structures. Examples can be observed in nature on different scales, and has also been found both numerically and experimentally.

Whorm-like channels can be formed dy dissolution in porous or fractured rock, governed by the coupling between fluid flow and chemical reactions at the rock surface [Szymczak and Ladd, 2006]. The channels will compete for the available flow, and the longer ones will have access to more chemical reactants than the shorter ones. Thus only the longer channels survive the competition, and the number of actively growing channels will decrease with time. Szymczak and Ladd used a resistor network model to study this interaction [Szymczak and Ladd, 2006].

When dendrites are formed by solidification from an undercooled solution, the advancing tip will have a stable parabolic shape. However, protrusions on its side walls will be unstable and grow into long fingers [Couder et al., 2005]. The evolution of these side-branches is deterministic, but the growth rate and length of a branch will depend on the size of the initial protrusion, and its position with respect to the neighbours. A screening effect by the longer branches will lead to a decay and eventually also stagnation in growth of the shorter ones. An example is shown in Fig. 9.1(b).

Recall from Sec. 2.3 that ECD experiments can be done with different

concentrations and a wide variety of chemical components, leading to patterns of diverse morphologies. Some experimental setups will lead to the formation of distinct, needlelike crystals of unlike lengths.

Zik and Moses did combustion experiments in Hele-Shaw geometry, with controlled amounts of fuel, oxidants and heat available to the flame [Zik and Moses, 1999]. In the regime of low oxidant flux, the initially flat combustion front will not propagate as a whole, but rather evolve into a number of fingers that will compete for the incoming flux. Fig. 9.1(a) is a nice illustration of the development of the interface. Once again, it is observed that when a finger grows slightly longer than its neighbours, it will have better growing conditions and therefore win the local contest.

Fluidisation experiments can be done by injecting air from the bottom of a vertical Hele-Shaw cell filled with glass beads [Nermoen, 2009]. If the granules are of different sizes, pipelike structures may be formed due to the sedimantation of bigger beads in the fluidised zones. An effective coarsening of the pattern lets only a few chimneys grow all the way to the top of the cell, see Fig. 9.1(c).

9.1 A model for fingered growth

These are just new examples of growth processes that may be modeled in terms of Laplacian growth. They all involve an initially planar or flat interface that evolves into a fingered pattern under the control of an harmonic field. The very first steps of this development will be the formation of small bumps or protrusions on the surface, nicely illustrated in Fig. 9.1(a). These shapes are well described in terms of linear (Mullins-Sekerka) stability analysis. However, when the initial bumps later grow into long fingers, this linear approximation is no longer valid.

The combustion, fluidisation, solidification and ECD experiments were all performed in Hele-Shaw cells or other quasi-two-dimensional geometries, which means that conformal mapping techniques may be used to study the observed interface evolutions. The models presented in

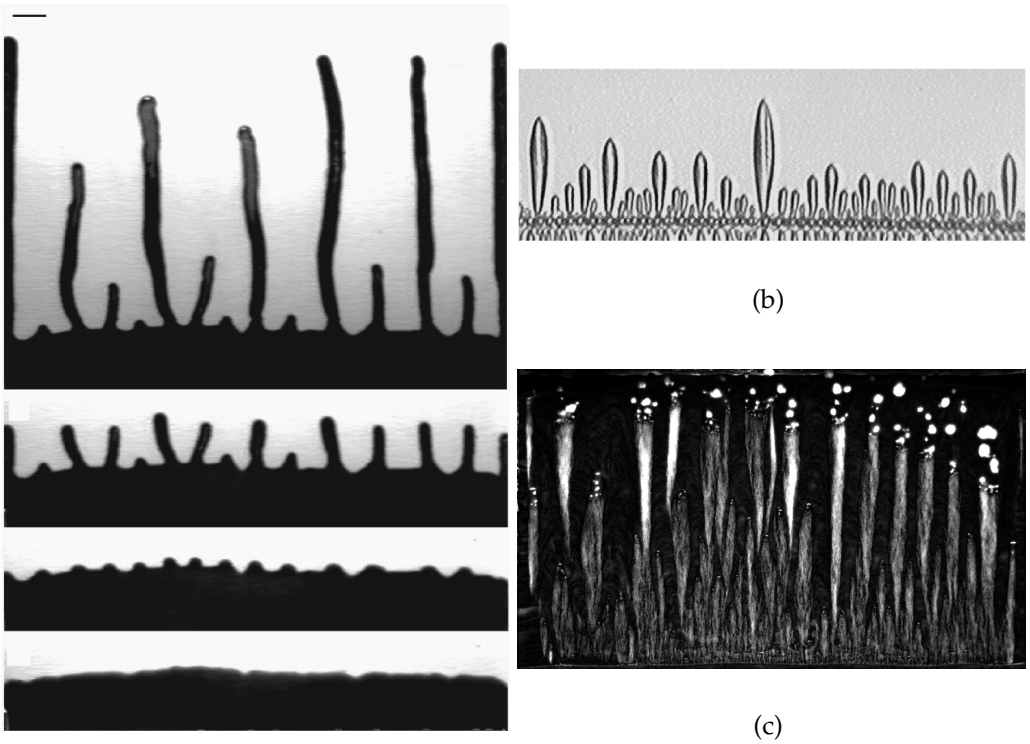

(a) (b) (c)

Figure 9.1: The images show examples of fingered growth in experiments. (a) shows how a combustion front evolves in time, starting out as a flat interface between flame and fuel and developing into a fingered pattern. From [Zik and Moses, 1999]. (b) illustrates how side-branches of dendrites have different lengths, depending on their position with respect to long and short neighbours [Couder et al., 2005]. (c) is a photograph of chimneys formed in fluidisation experiments where air is blown into a vertical Hele-Shaw cell filled with glass beads of different sizes (by [Nermoen, 2009]).

Chapter 7 were all based on the same idea: map the growing boundary onto the boundary of a mathematical reference domain, which has a geometry simple enough that the Laplace equation can easily be solved there. When using this method, one needs to keep close track of the evolution of the boundary, in order to at any instant be able to map it correctly to the reference domain. This involves quite a lot of analytics, which is why a nonlinear problem such as fingered growth is not easily handeled in this way. Therefore, a different model is used when studying this kind of surface evolution.

It is observed that the growth takes place mainly or only at the finger tips. This is an important simplification which implies that Loewner evolution could be a useful tool for solving this problem. Loewner's differential equation offers the opportunity to keep track of the evolution of the mapping of the boundary instead of the evolution of the boundary itself. This procedure keeps the analytics on an acceptable level.

Such a model was proposed by Selander in [Selander, 1999]. It assumes that a number of fingers are formed on the boundary due to a small initial perturbation. Once the fingers are formed, the further growth of the boundary takes place only at the finger tips. The system is totally deterministic: the initial positions of the finger tips code for their positions at any later time in the development. The competition between fingers that is observed in experiments is well described by the model. The gradient around the tip of a long finger will be larger than for a shorter one. Therefore longer fingers will grow faster and supress the growth of shorter, neighbouring fingers. The model assumes that all of the fingers have the same (small) width. The possibility of tip splitting or merging of fingers is neglected.

The model considers n (infinitely thin) fingers $\Gamma_i(t); i = 1, .., n$, that grow from the boundary and into the interior of a domain R. R can be e.g. the exterior of the unit circle, the upper half-plane, or an infinitely long channel. The parameter t represents the time, and the fingers are evolving in such a way that $\Gamma_i(t_1) \subset \Gamma_i(t_2)$ for $t_2 > t_1$. D denotes the domain R with the fingers subtracted, similar to what was described in Sec. 8.1.

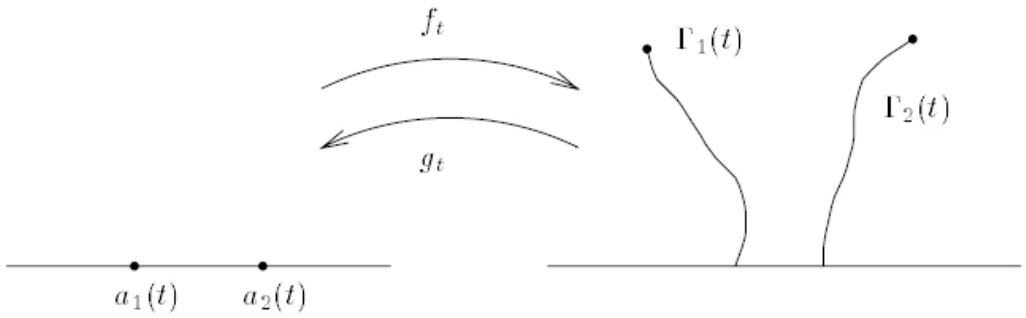

Figure 9.2: The figure is an illustration of the effect of the time dependent mapping g_t and its inverse f_t. The fingers $\Gamma_1(t)$ and $\Gamma_2(t)$ are growing into the interior of the reference domain. g_t map the finger tips to the points $a_1(t)$ and $a_2(t)$, respectively, on the boundary of the empty reference domain. The figure is obtained from [Selander, 1999].

When the fingers grow, the domain D will get smaller. As the fingers are infinitely thin, they actually coincide with the boundary of D. This is why it is enough to keep track of this boundary in order to model the finger growth.

The growth is controlled by the Laplacian field U, which satisfies the conformally invariant boundary condition $U = 0$ on the boundary of D; that is, on the boundary of R and along the fingers. Let g_t be a conformal map from D onto R, that maps the boundary of D onto the boundary of R. The inverse of g_t is denoted by f_t. g_t is constructed in such a way that the tip $\gamma_i(t)$ of the finger $\Gamma_i(t)$ is mapped to the point $a_i(t)$ in R by $a_i(t) = g_t(\gamma_i(t))$. The finger tip $\gamma_i(t)$ lies on the boundary of D, and hence $a_i(t)$ must lie on the boundary of R. The effect of the mappings g_t and f_t is illustrated for $n = 2$ in Fig. 9.2. Furthermore, the boundary condition $\frac{\partial U}{\partial y} \to 1$ as $y \to \infty$ is included, which ensures that there will be a constant flux at infinity. This flux should not be affected by the boundary movements, which means that the restriction $\lim_{z\to\infty} g_t(z) - z = 0$ must be added to g_t.

When the fingers grow, their tips will move around in space. g_t must therefore change in time in order to at any instant be able to map the finger

tips to the correct points on the boundary of R. g_t satisfies the Loewner differential equation, Eq. (8.2), which codes for this time change. Recall from Sec. 8.1 that the point $z = g_t^{-1}(a_i(t)) = \gamma_i(t)$ is the singularity of Eq. (8.2), and that the corresponding finger $\Gamma_i(t)$ is the trace of these singularities through time. g_t maps all the n fingers to the boundary of R simultaneously. Each finger $\Gamma_i(t)$ has its own set of values of $a_i(t)$ that controls its growth.

By using Darcy's law on the form of Eq. (5.10), it may be shown that the velocity $V_i(t)$ at each finger tip γ_i is related to the second derivative of the mapping f_t by

$$V_i(t) \sim |f_t''(a_i(t))|^{-\frac{\eta}{2}} \tag{9.1}$$

[Gubiec and Szymczak, 2008]. The interaction and competition between fingers will be dependent on the value of η and the geometry of R.

9.2 Fingered growth in the half-plane

The following model for n fingers growing in the upper half-plane was derived in [Selander, 1999]. It represents a simple way to study directional fingered growth, and it illustrates the competition between fingers for different values of η. The upper half-plane is a subset of the complex plane of coordinates $z = x + iy$, with the restriction $\mathtt{Im}\ z > 0$. The model provides a time dependent mapping f_t of the entire upper half-plane onto the half-plane with the fingers subtracted. The real axis (the boundary of the half-plane) is mapped to itself and the growing fingers.

Consider first a single finger growing into the half-plane. Recall from Sec. 8.3 that the discrete-time Loewner evolution of the conformal map f_t is represented by the composition $f_{t+\tau} = f_t \circ \varphi$, where φ adds a small increment to the finger tip in each time step. In this model the elementary map φ is on the form

$$\varphi(\omega) = a(t) + \sqrt{(\omega - a(t))^2 - 2\tau d(t)}, \tag{9.2}$$

where $d(t)$ is called the growth factor. From the discussion in Sec. 8.2 it is clear that $d(t)$ codes for how far the finger tip is moved parallel to the imaginary axis in each iteration.

Every time φ is applied, the finger will increase in length by approximately $\tau d(t)|f_t''(a(t))|$. Thus the velocity at the finger tip will be $V(t) = d(t)|f_t''(a(t))|$, which can be linked to Eq. (9.1) to show that the growth factor is given by

$$d(t) = |f_t''(a(t))|^{-1-\frac{\eta}{2}}. \tag{9.3}$$

For the n-finger case, each finger i has its own set of parameters a_i and d_i. Each time step includes a composition of n slit mappings φ_i, one for each finger: $f_{t+\tau} = f_t \circ \varphi_1 \circ \varphi_2 \circ ... \circ \varphi_n$. This means that the position $\gamma_i(t) = f_t(a_i(t))$ of the tip of one finger is dependent on the positions of all the other finger tips.

Due to Darcy's law, $V_n \sim |\nabla U|^\eta$, the fingers will always grow in the direction of the field gradient at their tip. For $n \geq 2$, $a_i(t)$ will be time dependent because of the interaction between the fingers. The point $a_i(t)$ is moved around on the real axis by all the elementary mappings φ_j; $j \neq i$, before it can code for the correct position $\gamma_i(t)$ of the i-th finger. This leads to a differential equation for the driving function:

$$\frac{d}{dt}a_i(t) = \sum_{\substack{j=1 \\ j\neq i}}^{n} \frac{d_j(t)}{a_i(t) - a_j(t)}.$$

When $n = 1$, $\frac{d}{dt}a(t) = 0$ and $a(t) = a(0)$ is a constant, which means that the single finger is a straight line growing from the point $a(0)$ on the real axis. This follows naturally from symmetry arguments: With no competing fingers to change the direction of the gradient line around the single finger, it will always grow perpendicularly to the real axis.

For $n \geq 2$, the behaviour of the fingers is very sensitive to the value of the parameter η in Eq. (9.3). Gubiec and Szymczak claims that there are three different regimes in the growth of the fingers: the growth is

stable for low values of η and unstable for high values, in addition to an intermediate metastable state [Gubiec and Szymczak, 2008]. Carleson and Makarov studied a similar growth model and showed that the values of η at which the transition between the regimes takes place is dependent on the number of fingers [Carleson and Makarov, 2002]. The total number of fingers is of importance in the model used here too, but it is observed that the density of fingers seems to be significant for the local growth behaviour for a wide range of values of η.

Stable growth means that there is little or no competition between the fingers, such that they all grow with more or less the same speed. Note that when $\eta = -2$, the growth factor in Eq. (9.3) is a constant. This gives stable growth for any number of fingers, provided that they do not grow too close to each other. Fig. 9.3(a) shows an example of stable growth of two fingers in the half-plane: they have the same speed and angle with respect to the real axis. In the metastable regime, some of the fingers will grow faster than the others such that there will be a screening effect. However, the screening is only partial and thus the ratio of the tip velocities in metastable growth will converge towards a constant value. Finally, in the unstable regime one or more of the fingers will soon grow longer than its neighbours, and there will be a complete screening. In the very end only one finger will survive. Fig. 9.3(b) shows an example of the development of two fingers in the unstable regime.

Fig. 9.4 illustrates the step-by-step evolution of the fingers due to their internal competition. The figure shows five fingers growing at $\eta = 1$, and is a particularly nice example of how the density of fingers determine which stability regime the local growth belongs to. Denote the fingers by numbers, such that the leftmost one is finger 1 and the one to the very right is finger 5. Concentrate first on finger 1 and 2: they are not much affected by the three fingers on the right hand side. Their behaviour looks almost as if they were growing isolated from the other ones (compare to Fig. 9.4); only the slightly smaller angle between them gives away that they are not growing alone. Their growth is an example of the metastable state, where finger 1 clearly takes over control, but without killing finger

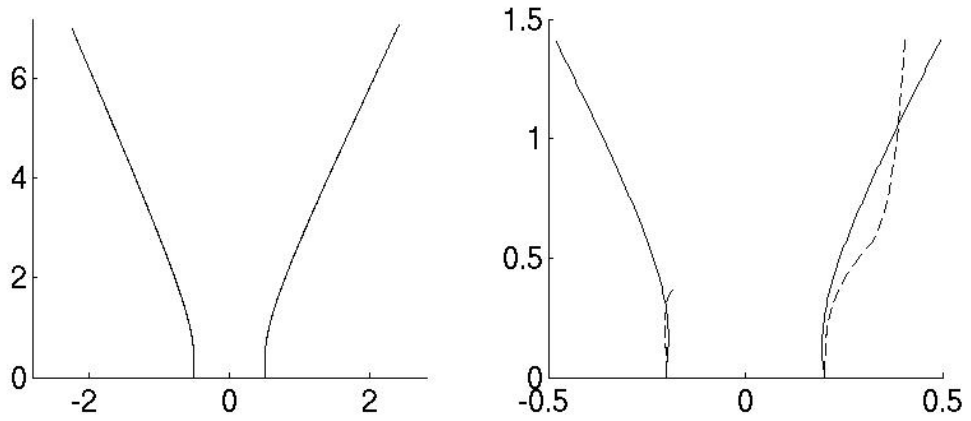

(a) (b)

Figure 9.3: The figure shows two fingers growing in the half-plane for different values of η. In (a), $\eta = 1$ and the growth is stable. The fingers cooperate rather than compete, and bend away from each other such that both of them have the most ideal conditions. The initial positions are $a_1(0) = -0.5$ and $a_2(0) = 0.5$. (b) shows a comparison between stable and unstable growth. The fingers plotted with a solid line are grown at $\eta = -1$, whereas the ones in dashed lines belong to the unstable regime, at $\eta = 4$. The unstable fingers have a larger influence on each other from the very beginning, with a stronger repelling effect than for $\eta = -1$. At the instant when one of the fingers gets slightly longer than the other (due to numerical noise), its growth velocity will increase dramatically, and the shorter finger will soon die out. The initial positions are $a_1(0) = -0.2$ and $a_2(0) = 0.2$

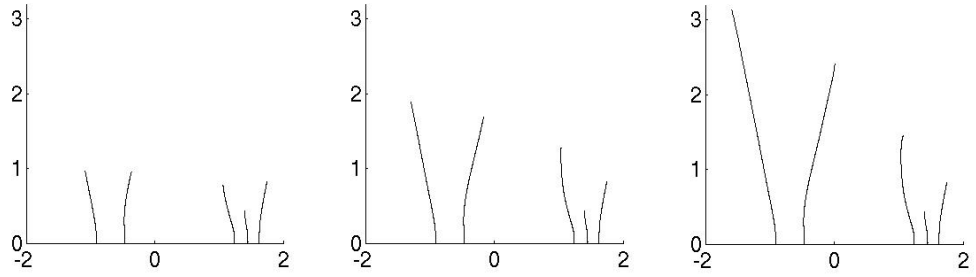

Figure 9.4: Five fingers growing in the half-plane for $\eta = 1$. The initial positions are chosen randomly in the range $[-2.5, 2.5]$. The figure shows how the fingers affect each other and how the local density of fingers is important for their behaviour. The simulation starts at time $t = 0$, and the plots are made at times t_a, $t_b = 2t_a$ and $t_c = 3t_a$.

2 completely. The three fingers on the right hand side are much closer to each other, and their growth is unstable. There is a strong screening which leads to a successive killing of the shortest fingers. The single finger that finally remains is soon killed by its two neighbours to the left. Somewhat surprising is the observation that finger 3, which wins the internal competition between fingers 3, 4 and 5 (Fig. 9.4(c)), is not the longest one of these in the beginning (Fig. 9.4(a)).

9.3 Fingered growth in channel geometry

Many of the experiments on finger growth are done in Hele-Shaw cells, which means that the side walls of the cell will have an effect on the evolution of the interface. The model for fingered growth in the half-plane does not take this effect into account. A new model will be presented in this section, in which the side walls and their boundary effects are included. The model has only small modifications with respect to the one by Gubiec and Szymczak, and the details of the derivation can be found

in Ref. [Gubiec and Szymczak, 2008].

The growth now takes place in a channel with impenetrable and reflecting side walls. The channel is a subset of the complex plane with coordinates $z = x + iy$, and lies in the upper half-plane ($\mathtt{Im}\ (z) > 0$) between $x = -1$ and $x = 1$. As in the half-plane model, the boundary condition at the bottom wall $y = 0$ is $U = 0$. It is supplied by the criterion $\frac{\partial U}{\partial x} = 0$ at the side walls $x = \pm 1$. The goal is to derive a mapping f_t from the empty channel onto the channel with the growing fingers subtracted.

The side walls must remain fixed under the mapping f_t, which means that the slit map in the entire upper half-plane (Eq. (9.2)) must be modified. The slit mapping φ in channel geometry has the form

$$\varphi(\omega) = \frac{2}{\pi} \arcsin \left[\varpi + \frac{1}{2} \sqrt{\left[\tilde{\varphi}^- \sin(\frac{\pi}{2}\omega) + \tilde{\varphi}^+ - 2\varpi \right]^2 - 8\tau d'} \right],$$

with the abbreviations

$$d' = d\frac{\pi^2}{4} \cos^2(\frac{\pi}{2}a),$$

$$\varpi = (1 + \frac{\pi^2}{4}\tau d) \sin(\frac{\pi}{2}a),$$

$$\tilde{\varphi}^- = \tilde{\varphi}(1) - \tilde{\varphi}(-1),$$

$$\tilde{\varphi}^+ = \tilde{\varphi}(1) + \tilde{\varphi}(-1),$$

$$\tilde{\varphi}(x) = \varpi + \sqrt{\left[\sin(\frac{\pi}{2}x) - \varpi \right]^2 + 2\tau d'}.$$

Also here, the n-finger case is analyzed by a composition of n slit mappings φ_i, one for each finger i. The growth factor $d_i(t)$ is independent on the geometry and is therefore still related to η and the mapping f_t by $d_i(t) = |f_t''(a_i(t))|^{-1-\frac{\eta}{2}}$, exactly as in the half-plane. However, as explained in the previous section, the driving functions $a_i(t)$ are influenced by the elementary mappings φ_j. As φ_j is on another form in this geometry than in the half-plane, the differential equation for $a_i(t)$

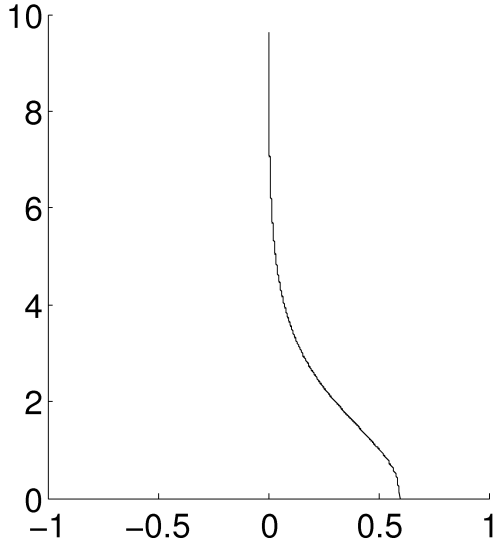

Figure 9.5: The shape of a single finger in channel geometry will be independent on the value of η. The channel has reflecting sidewalls, and this effect makes the finger grow towards the center of the channel, regardless of its initial position.

needs a modification. The new relation is

$$\frac{d}{dt}a_i = -\frac{\pi}{4}d_i \tan(\frac{\pi}{2}a_i) + \frac{\pi}{2}\sum_{\substack{j=1 \\ j\neq i}}^{n} d_j \frac{\cos(\frac{\pi}{2}a_i)}{\sin(\frac{\pi}{2}a_i) - \sin(\frac{\pi}{2}a_j)}. \tag{9.4}$$

When $n = 1$, only the self term $\frac{d}{dt}a(t) = -\frac{\pi}{4}d(t)\tan(\frac{\pi}{2}a(t))$ of Eq. (9.4) remains. It makes the derivative $\frac{d}{dt}a(t) \neq 0$ whenever $a(t) \neq 0$, which means that $a(t)$ is nonconstant as long as it is away from the center of the channel. A nonconstant driving function will give a curved trace Γ_t. The reflecting sidewalls will make the single finger grow towards the center of the channel, and once it hits the centerline, $\frac{d}{dt}a(t) = 0$, and the finger will continue its growth along the centerline. Fig. 9.5 shows this behaviour of a single finger growing in channel geometry. When $n \geq 2$, there will be a competition between the fingers, and the self term now only acts on the winning finger to attract it to the centerline when the growth of the losing fingers has ceased.

For $n = 1$ it has already been shown that the shape of the finger is independent on η. Only the velocity of the finger tip will be affected when changing η, due to Eq. (9.1). For $n \geq 2$ the value of η plays

a significant role for the growth of the fingers also in this geometry. η controls the interaction between the fingers in the same manner as in the half-plane. Fig. 9.6 shows how the growth of two fingers will be modified when tuning η. The three growth regimes that were discussed in Sec. 9.2 are observed also here. The left plot shows stable growth. The two fingers repel each other with equal strength, such that they seek towards the positions ± 0.5. This behaviour admits both of them to have the best possible growth conditions at the same time. The plot in the middle is an example of metastable growth, where there is some competition between the fingers. The winning finger grows towards the center of the channel and pushes the other away, but the losing finger does not completely stop growing. The plot to the right shows the unstable regime, where the winning finger is attracted to the center of the channel once the other one has been killed.

9.4 Comments on numerics

Writing the map of the finger tips as a composition of elementary maps is in many ways a simplification with respect to a direct integration of the Loewner differential equation. However, in these two models for fingered growth, complications arise when it comes to computing the growth factor $d_i(t) = |f_t''(a_i(t))|^{-1-\frac{\eta}{2}}$. If the second derivative of an iterated map is to be found analytically, it requires a combination of the chain- and product rule for differentiation. For n fingers at time t, this includes an intricate combination of the first and second derivatives of $n\frac{t}{\tau}$ elementary maps with individual parameters a_i and d_i. A purely analytic algorithm for finding the growth factor is therefore quite cumbersome to implement. For simplicity, a combination of analytic and numeric differentiation is used: the first derivative is computed analytically at the points $a_i(t)$ and $a_i(t) + \varepsilon$, and the results are then used to compute the second derivative by $f_t''(a_i(t)) = \frac{f_t'(a_i(t)+\varepsilon) - f_t'(a_i(t))}{\varepsilon}$. The method is not very sophisticated, but it is sufficient for these purposes.

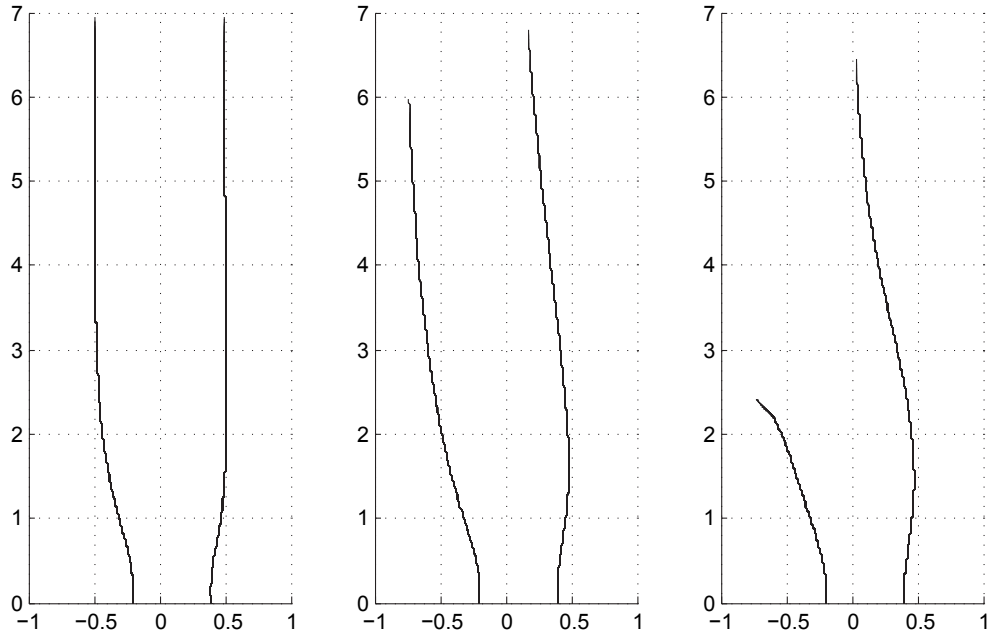

Figure 9.6: The figure shows how the parameter η in Eqs. (9.1) and (9.3) affects the competition between two fingers growing in a channel. When $\eta = -2$ (left), the growth factor is a constant and the fingers do not compete: they grow towards the position in the channel that gives both of them as much influx as possible. For $\eta = 0$ (middle) and $\eta = 1$ (right), there is a competition between the fingers, and the winning finger will grow towards the center of the channel, where most incoming flux is available.

The initial positions of the fingers are sometimes chosen randomly. The random numbers are then generated from a uniform distribution, in the channel between -1 and 1 and for n fingers in the half-plane between $-\frac{n}{2}$ and $\frac{n}{2}$.

Slow fingers may generate numerical instabilities due to small number computations. To avoid this, fingers growing slower than a certain threshold value are killed. Slow fingers still affect its neighbours, and must therefore remain in the computations. Killing a finger therefore only means that its position in every new time step after the killing is set equal to the last position it had before it was killed.

Chapter 10

Critical phenomena

The correlation function $G(r, \xi)$, with the corresponding correlation length ξ, is used as a description of the degree of order in a system. It describes how strongly physical observables at different positions are related to each other, as a function of the distance r between the positions. One might think of this as a measure of the degree of order in a system. For a d-dimensional system, the correlation function can be expressed as

$$G(r, \xi) = \frac{1}{r^{d-2+\wp}} e^{-\frac{r}{\xi}}$$

where $\wp$ is a critical exponent that is introduced to make sure that $G(r, \xi)$ shows the correct behaviour as $\xi \to \infty$. $\wp$ can have different positive values, dependent on the problem at hand.

The order or disorder in a system is usually dependent on the temperature T. In this case the correlation length is given by $\xi = \xi_0 |T - T_c|^{-\upsilon}$. At the critical temperature T_c the correlation length diverges, and the system no longer possesses a characteristic length scale. When the temperature passes through T_c, the system undergoes a second order phase transition (i.e. a phase transition in which no latent heat is involved). At this critical temperature, the system shows special behaviours called critical phenomena.

10.1 Scaling and universality

A common example of a system that exhibits temperature dependent ordering and a second order phase transition at some critical temperature is the Ising spin model. It is a lattice on which the spin σ_i at each lattice point i can take one of the values $\sigma_i = \pm 1$. At $T = 0$, the system is totally ordered: it takes on a ferromagnetic ground state with all the spins aligned. As T increases the system remains ferromagnetic with long range order: clusters of characteristic size $\xi(T)$ have equally oriented spins, with small intermediate islands of oppositely directed spins. As T approaches T_c, observable physical properties behave as $O(T) \propto (T - T_c)^{\nu_O}$, where ν_O is an exponent characteristic for each observable. At the critical point the correlation length and the observables diverge, meaning that this description of the system breaks down. Above the critical point the system is in a paramagnetic state without long range order, but with clusters of characteristic size $\xi(T)$ in which the spins are ordered. As $T \to \infty$, $\xi \to 0$, and the system is totally disordered.

The diverging correlation length at T_c implies that the system becomes scale invariant at the critical point. This means that the system will look exactly the same at every length scale up to the system size: it is invariant under rescaling. This property applies to both the system geometry and to physical properties and measures on the system. It further implies that the system has a fixed point at T_c. The geometric interpretation of scale invariance is that clusters of equally aligned spins make up a self-similar structure. Moreover, the scaling of the observables around T_c exhibit an intriguing behaviour called universality: regardless of the specifications of the system at hand, the exponents ν_o will take on the same value for very different systems.

10.2 Conformal invariance

At the critical point, and at length scales much larger than the distance between lattice points, the lattice representation of spins can be replaced

by a continuum model. The spins are then described by a local field $\Psi(r)$ which is also scale invariant. This scale invariance has further important implications for the system at the critical point. The geometry in the continuum limit of a self-similar structure will be independent on translation, rotation and magnification, which means that the system is conformally invariant. The continuum theory therefore falls into the category of conformal field theories.

The behaviour of the Ising model at the critical point is not unique. It can be shown that many other statistical mechanics lattice models, such as percolation and random walks, also have these properties.

The conformal invariance is valid not only for the geometry of the system, but also for probability measures. Consider a lattice model in the continuum limit theory, and let D_1 and D_2 be two domains on the lattice. The curve ℓ connects two points on the boundary of D_1, and the probability measure on ℓ is $P_{D_1}(\ell)$. By the Riemann mapping theorem, D_1 can be mapped conformally onto D_2 by means of a transformation $g(D_1)$, and it follows that the curve on the interface maps to $g(\ell)$. The scale invariance that leads to conformal invariance then states that the probability measure is invariant under this transformation, i.e $P_{D_1}(\ell) = P_{D_2}(g(\ell))$.

10.3 Stochastic Loewner Evolution

In 2000, Oded Schramm took Loewner evolution one step further by introducing a stochastic driving function $a(t)$ in Eq. (8.2) [Schramm, 2000]. As was seen in Sec. 8.2, a continuous driving function yields a continuous trace γ_t in the z-plane. Scramm realised that if $a(t)$ is a continuous random function then the trace will be a random curve. The study of the Loewner equation with a stochastic driving function is called Stochastic Loewner Evolution (SLE). It can be used to study two-dimensional critical phenomena.

In SLE, the driving function is given by a Gaussian distribution

$$P(a,t) = \frac{1}{\sqrt{2\pi t}} e^{-\frac{a^2}{2\aleph t}}$$

satisfying the correlations

$$\langle (a(t) - a(\zeta))^2 \rangle = \aleph |t - \zeta|,$$

where the braces denote the variance. $\aleph$ is a dimensionless parameter that is very important for the behaviour of the trace γ_t. Schramm showed that if $a(t)$ further satisfies the restrictions of Brownian motion, then SLE would produce a conformally invariant, fractal trace γ_t.

For $0 < \aleph \leq 4$ the trace is a simple random curve that does not intersect itself nor the real line. Different examples of critical phenomena can be connected to special values of $\aleph$. As an example, $\aleph = 3$ yields a trace that has been conjectured to correspond to the spin cluster boundaries of the Ising model at the critical temperature T_c [Gruzberg and Kadanoff, 2004]. For $4 < \aleph < 8$, the trace starts intersecting itself. This leads to "holes" in the domain D, which violates the Riemann mapping theorem which is applicable to simply connected domains only. Thus, each time the trace intersects itself the enclosed hull is removed from D. There are theorems stating that also these hulls can be used to describe different properties of critical phenomena. When $\aleph \geq 8$ the trace fills a whole region. Fig. 10.1 shows examples of boundary curves in critical phenomena that correspond to SLE traces for $\aleph = 2$ and $\aleph = 8$.

It was shown in [Rohde and Schramm, 2005] that the Hausdorff dimension D_H of the curve generated by SLE is dependent on $\aleph$ through

$$D_H = 1 + \frac{\aleph}{8} \qquad \texttt{for } 0 \leq \aleph \leq 8.$$

For $\aleph \geq 8$ the curve fills a part of the plane and D_H locks onto 2.

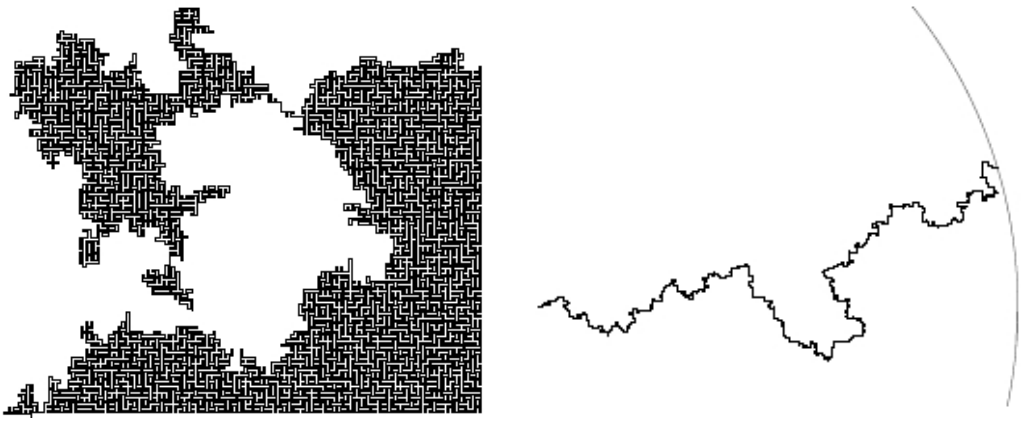

(a) (b)

Figure 10.1: Examples of conformally invariant paths that correspond to SLE traces for different values of $\aleph$. (a) is a uniform spanning tree Peano curve. The curve is space filling, and converges to an SLE with $\aleph = 8$. (b) shows a loop-erased random walk from the center to the rim of a disc, and has been shown to represent SLE with $\aleph = 2$. The figures are obtained from [Schramm, 2006].

Chapter 11

Summary

Much work has been devoted to the study of non-equilibrium growth phenomena, and the effort has lead to the establishment of a variety of growth models. Laplacian growth represents a very simple model that can be used to study surprisingly complex, fractal structures. As a fundamental model it may be used as a tool to gain further insight into many different problems; both well known and newer ones. Due to the invention of new modeling techniques and the exploration of previously unknown phenomena in physics, new applications of the model steadily appear.

The Loewner equation has recently been connected to Laplacian growth in order to easily study directional fingered growth, which is complicated to solve with the classical conformal mapping techniques. The iterated conformal maps technique has already been used to study different types of boundary evolution, and is the key to why the Loewner equation can be applied to the fingered growth phenomenon. This is indeed an ingenious way to reproduce many of the fingered patterns that can be observed in experiments and in the field. However, the model as it is presented here has some weaknesses and needs to be improved before it can be tied up to any of these examples.

The Loewner equation has applications far beyond solving boundary evolution problems. It was introduced in 1923 to solve the Bieberbach

conjecture, and reentered the research frontier when Schramm coupled it to Brownian motion in 2000. Many of the conjectures made on SLE in connection to critical phenomena are still not proven.

The aim of this thesis has been to tie together some well established and newer approaches to the study of Laplacian growth. Non-equilibrium growth phenomena on unstable surfaces has been the red line, and this will represent a current research topic as long as the fascination for the structures that it produces is still alive.

Appendix A

Derivation of the conformal map $f(\omega)$

The mapping $f(\omega)$ of the exterior of the unit circle onto a nearly circular domain, perturbed by the function $h(\theta) = \epsilon \cos(m\theta)$, was an important ingredient in the study of growth phenomena in radial geometry. This is a summary of a derivation of $f(\omega)$, obtained from [Nehari, 1982].

A.1 Gauss' theorem

Let D be a domain bounded by a piecewise smooth curve Λ, and take two functions $p(x, y)$ and $q(x, y)$ that both are continuous and have continuous first partial derivatives in D. Gauss'theorem then states that

$$\iint_D \left[\frac{\partial p}{\partial x} + \frac{\partial q}{\partial y}\right] dx\, dy = \int_\Lambda \left[p(x, y)dy - q(x, y)dx\right] \tag{A.1}$$

If $u(x, y)$ and $v(x, y)$ are functions with continuous first and second partial derivatives in D and Λ, then

$$p(x, y) = u\frac{\partial v}{\partial x} \quad \texttt{and} \quad q(x, y) = u\frac{\partial v}{\partial y}$$

satisfy the requirements of Gauss' theorem. Eq. (A.1) can then be rewritten as

$$\iint_D \left[\frac{\partial u}{\partial x}\frac{\partial v}{\partial x} + u\frac{\partial^2 v}{\partial x^2} + \frac{\partial u}{\partial y}\frac{\partial v}{\partial y} + u\frac{\partial^2 v}{\partial y^2}\right] dxdy = \int_\Lambda u\big[\frac{\partial v}{\partial x}dy - \frac{\partial v}{\partial y}dx\big]. \quad \text{(A.2)}$$

The line integral in Eq. (A.2) can be simplified by introducing differentiation in the direction of the outward pointing normal of Λ:

$$\frac{\partial v}{\partial n} = \frac{\partial v}{\partial x}\cos(x,n) + \frac{\partial v}{\partial y}\cos(y,n),$$

where (x,n) and (y,n) are the angles between the normal and the positive $x-$ and $y-$axis, respectively. By using the direction cosines of the tangent corresponding to the normal, it can be shown that $\cos(x,n) = \frac{dy}{ds}$ and $\cos(y,n) = -\frac{dx}{ds}$, where s is the arc-length parameterisation of Λ. The relation

$$\frac{\partial v}{\partial n}ds = \frac{\partial v}{\partial x}dy - \frac{\partial v}{\partial y}dx$$

is then obtained. This, together with the fact that $\nabla^2 v = \Delta v = \frac{\partial^2 v}{\partial x^2} + \frac{\partial^2 v}{\partial y^2}$, brings Eq. (A.2) onto the form

$$\iint_D u\Delta v\, dx\, dy + \iint_D \left[\frac{\partial u}{\partial x}\frac{\partial v}{\partial x} + \frac{\partial u}{\partial y}\frac{\partial v}{\partial y}\right] dxdy = \int_\Lambda u\frac{\partial v}{\partial n}ds, \quad \text{(A.3)}$$

which is called *Green's first formula*. Swapping u and v in Eq. (A.3), then subtracting the two equations from eachother, gives us *Green's second formula*:

$$\iint_D (u\Delta v - v\Delta u)\, dx\, dy = \int_\Lambda \Big(u\frac{\partial v}{\partial n} - v\frac{\partial u}{\partial n}\Big) ds. \quad \text{(A.4)}$$

Observe that if both $u(x,y)$ and $v(x,y)$ are harmonic, then

$$\int_\Lambda \Big(u\frac{\partial v}{\partial n} - v\frac{\partial u}{\partial n}\Big) ds = 0. \quad \text{(A.5)}$$

A.2 The Green's Function

Let the function $w(x, y)$ be harmonic in D and have continuous first partial derivatives in D and Λ. Take a point $(\varkappa, \iota)$ inside D; then the distance between (x, y) and $(\varkappa, \iota)$ is $r_i = \sqrt{(x-\varkappa)^2 + (y-\iota)^2}$ and $\log r_i$ is harmonic in D and Λ except at the point $(\varkappa, \iota)$. Then the function

$$k(x, y) = w(x, y) - \log r_i$$

will also be harmonic exactly where $\log r_i$ is. Since $k(x, y)$ is not harmonic at the point $(\varkappa, \iota)$ in D, introduce the new domain D_ϵ, which is bounded by Λ and a circle C_ϵ of radius ϵ with center at $(\varkappa, \iota)$. If $u(x, y)$ is harmonic in D, then Eq. (A.5) becomes

$$\int_\Lambda \Big(u\frac{\partial k}{\partial n} - k\frac{\partial u}{\partial n}\Big)ds - \int_{C_\epsilon} \Big(u\frac{\partial k}{\partial n} - k\frac{\partial u}{\partial n}\Big)ds = 0. \tag{A.6}$$

as the boundary of D_ϵ is to be traversed in such a way that the interior always stays on ones left side. With C_ϵ being a circle, one can conviniently write the rightmost integral in Eq. (A.6) in polar coordinates ($(x, y) \rightarrow (r, \theta)$):

$$\int_{C_\epsilon} \Big(u\frac{\partial k}{\partial n} - k\frac{\partial u}{\partial n}\Big)ds = \int_{C_\epsilon} \left[u\Big(\frac{\partial w}{\partial r} - \frac{1}{r}\Big) - (w - \log r_i)\frac{\partial u}{\partial r}\right] r d\theta$$

$$= -\int_0^{2\pi} u d\theta + \epsilon \int_0^{2\pi} \Big(u\frac{\partial w}{\partial r} - w\frac{\partial u}{\partial r}\Big)d\theta + \epsilon \log \epsilon \int_0^{2\pi} \frac{\partial u}{\partial r}.$$

In the limit $\epsilon \rightarrow 0$ the two last integrals vanish. The remaining integral equals $2\pi u(\varkappa, \iota)$, by the mean value theorem. Eq. (A.6) then becomes *Green's third formula*:

$$\int_\Lambda \Big(u\frac{\partial k}{\partial n} - k\frac{\partial u}{\partial n}\Big)ds + 2\pi u(\varkappa, \iota) = 0. \tag{A.7}$$

The usefulness of this formula is obvious when $k(x, y)$ is replaced by the *Green's function* of the domain, which has the form

$$G(x, y; \varkappa, \iota) = \tilde{G}(x, y; \varkappa, \iota) - \log r_i, \tag{A.8}$$

where $r_i = \sqrt{(x-\varkappa)^2 + (y-\iota)^2}$ and $\tilde{G}$ is harmonic in D. When (x, y) tends to Λ, then the Green's function tends to zero.

As Eq. (A.7) is a line integral over the boundary of D, the right hand term in the integral wanishes due to the properties of the Green's function. What remains is

$$u(\varkappa, \iota) = -\frac{1}{2\pi} \int_\Lambda u \frac{\partial G}{\partial n}\, ds. \tag{A.9}$$

This means that if the Green's function of a domain (and its derivative) is known, all you need is the boundary values of the function $u(x, y)$, and thereby you can compute the values of u in any other point in the domain.

A.3 The Green's function of a circle

Let now D be the circle $C_\mathcal{R}$ of radius $\mathcal{R}$ and with center at the origin. Using polar coordinates (r, θ), the Green's function of this domain with respect to the point $(\nu, \vartheta); \nu < \mathcal{R}$ reads

$$G_{C_\mathcal{R}}(x, y; \varkappa, \iota) = \frac{1}{2} \log \frac{\mathcal{R}^2 - 2\nu r \cos(\theta - \vartheta) + \frac{\nu^2 r^2}{\mathcal{R}^2}}{r^2 - 2\nu r \cos(\theta - \vartheta) + \nu^2} \tag{A.10}$$

To verify this formula, rewrite it as

$$G(x, y; \varkappa, \iota) = -\log r_1 + \log r_2 + \log \frac{\nu}{\mathcal{R}}$$

where

$$r_1^2 = r^2 - 2\nu r \cos(\theta - \vartheta) + \nu^2$$

is the distance from the point (x, y) to $(\varkappa, \iota)$ and

$$r_2^2 = r^2 - 2\frac{\mathcal{R}^2 r}{\nu} \cos(\theta - \vartheta) + \frac{\mathcal{R}^4}{\nu^2}$$

is the distance from (x, y) to the point inverse to $(\varkappa, \iota)$ with respect to the boundary of $C_{\mathcal{R}}$, having the polar coordinates $(\frac{\mathcal{R}^2}{\nu}, \vartheta)$.

It is easy to show that when r_i is the distance between two points (x, y) and $(\varkappa, \iota)$ in D, then $\log r_i$ is harmonic in D except at $(x, y) = (\varkappa, \iota)$. Therefore, $G(x, y; \varkappa, \iota)$ is also harmonic in D except at $(\varkappa, \iota)$. Set $r = \mathcal{R}$ in Eq. (A.10) to verify that it is zero on the boundary of the domain; all the requirements of the Green's function are satisfied.

A.4 The variation formula

Let D be subject to a small perturbation h that changes it into the new domain D^h. The Green's function and boundary of D^h are denoted by $G^h(x, y; \varkappa, \iota)$ and Λ^h, respectively. Recall that s is the arc-length parameter for Λ. Construct a normal at every point $z(s)$ along Λ; the distance along the normal from $z(s)$ until its intersection point $z^h(s)$ with Λ^h is denoted by $\delta n(s)$. Let ϵ be a small number; then $\delta n(s) = \epsilon \hat{h}(s) = h(s)$ satisfies the requirement that the perturbation be small.

It can be shown that the variation of the Green's function due to the perturbation is expressed by

$$\delta G(x, y; \varkappa, \iota) = G^h(x, y; \varkappa, \iota) - G(x, y; \varkappa, \iota)$$

$$= \frac{1}{2\pi} \int_{\Lambda} \frac{\partial G(\chi, \zeta; x, y)}{\partial n} \frac{\partial G(\chi, \zeta; \varkappa, \iota)}{\partial n} \delta n(s)\, ds + o(\epsilon). \tag{A.11}$$

Using this *variation formula* and Eq. (A.10), the Green's function of a nearly circular domain can be found. Changing again into polar coordinates, where $(x, y) \to (r, \theta)$, $(\varkappa, \iota) \to (\nu, \vartheta)$ and $(\chi, \zeta) \to (\xi, \phi)$, gives

$$\delta G(x, y; \varkappa, \iota) = \frac{(r^2 - \mathcal{R}^2)(\nu^2 - \mathcal{R}^2)}{2\pi\mathcal{R}}$$

$$\int_0^{2\pi} \frac{\delta n(\phi)\, d\phi}{(\mathcal{R}^2 - 2r\mathcal{R}\cos(\phi - \theta) + r^2)(\mathcal{R}^2 - 2\nu\mathcal{R}\cos(\phi - \vartheta) + \nu^2)} + o(\epsilon)$$

Let $(\varkappa, \iota)$ be the origin; then $\nu = 0$ and Eq. (A.10) simlifies to $\log \frac{\mathcal{R}}{r}$, and

the Green's function of the nearly circular domain, whose boundary is determined by the equation $\mathcal{R} + h(\theta)$, reads

$$G^h_{C_\mathcal{R}}(x, y; 0, 0) = G_{C_\mathcal{R}}(x, y; 0, 0) + \delta G_{h(\theta)}(x, y; 0, 0)$$

$$= \log \frac{\mathcal{R}}{r} + \frac{(\mathcal{R}^2 - r^2)}{2\pi\mathcal{R}} \int_0^{2\pi} \frac{\epsilon \hat{h}(\phi)\, d\phi}{\mathcal{R}^2 - 2r\mathcal{R}\cos(\phi - \theta) + r^2} + o(\epsilon) \qquad \text{(A.12)}$$

A.5 Green's functions and maps

It can be shown that if the function $g(x, y; \varkappa, \iota)$ maps the domain D onto the unit circle, and brings the point $(\varkappa, \iota)$ to the origin, then

$$G(x, y; \varkappa, \iota) = -\mathtt{Re}\big[\log\big(g(x, y; \varkappa, \iota)\big)\big] = -\log|g(x, y; \varkappa, \iota)| \qquad \text{(A.13)}$$

is the Green's function of D. We already found an expression for the Green's function of both a circle and a nearly circular, perturbed domain. Then we are able to find an explicit expression for the map between them, using Eq. (A.13).

Let now D be a simply-connected, nearly circular domain with boundary $r = 1 + \epsilon\hat{h}(\theta)$. $\hat{h}(\theta)$ is a bounded and piecewise continuous function, and ϵ is a small, positive parameter, small enough that second order terms can be neglected. Introduce $z = re^{i\theta}$; then Eq. (A.12) can be rewritten as

$$G^h_{C_1}(x, y; 0, 0) = -\log|z| + \frac{(1 - r^2)}{2\pi} \int_0^{2\pi} \frac{\epsilon \hat{h}(\phi)\, d\phi}{1 - 2r\cos(\phi - \theta) + r^2} + o(\epsilon)$$

$$= \mathtt{Re}\left(-\log z + \frac{\epsilon}{2\pi} \int_0^{2\pi} \frac{e^{i\phi} + z}{e^{i\phi} - z} \hat{h}(\phi)\, d\phi \right) + o(\epsilon).$$

Relating this to Eq. (A.13) gives the final formula for the map:

$$g(z) = z - \frac{\epsilon z}{2\pi} \int_0^{2\pi} \frac{e^{i\phi} + z}{e^{i\phi} - z} \hat{h}(\phi)\, d\phi + o(\epsilon) \qquad \text{(A.14)}$$

Now that the map $\omega = g(z)$ onto the unit circle is found, it is desirable to compute its inverse; $z = f(\omega)$; the mapping from the unit circle onto a nearly circular domain. $g(z)$ has the more generalized form $g(z) = z - \epsilon\hat{h}(z) + o(\epsilon)$, so assume that $f(\omega)$ looks like $f(\omega) = \omega + \epsilon\hat{k}(\omega) + o(\epsilon)$. Inserting one into the other shows that $\hat{h} = \hat{k}$, and the inverse function must be

$$f(\omega) = \omega + \frac{\epsilon\omega}{2\pi}\int_0^{2\pi} \frac{e^{i\phi} + \omega}{e^{i\phi} - \omega}\hat{h}(\phi)\, d\phi + o(\epsilon) \tag{A.15}$$

Eq. (A.15) maps the interior of the unit circle onto the perturbed domain. We want instead to consider the exterior, which means that the integration is to be done around infinity, and not around the origin:

$$f(\omega) = \omega + \frac{\epsilon\omega}{2\pi}\int_0^{2\pi} \frac{e^{-i\phi} + \omega}{e^{-i\phi} - \omega}\hat{h}(-\phi)\, d\phi + o(\epsilon) \tag{A.16}$$

Let the perturbation $h(\theta) = \epsilon\cos(m\theta)$; then Eq. (A.16) simplifies to

$$f(\omega) = \omega + \epsilon\omega^{-m+1}. \tag{A.17}$$

Bibliography

[Barra et al., 2001a] Barra, F., Davidovitch, B., Levermann, A., and Procaccia, I. (2001a). Laplacian growth and diffusion limited aggregation: Different universality classes. *Phys. Rev. Lett.*, 87(13):134501.

[Barra et al., 2001b] Barra, F., Davidovitch, B., and Procaccia, I. (2001b). Iterated conformal dynamics and Laplacian growth. *Phys. Rev. E*, 65.

[Bauer and Bernard, 2006] Bauer, M. and Bernard, D. (2006). 2D growth processes: SLE and Loewner chains. *Physics Reports*, 432.

[Bazant and Crowdy, 2005] Bazant, M. Z. and Crowdy, D. G. (2005). Conformal mapping methods for interfacial dynamics. In *Handbook of Materials Modelling*. Springer.

[Brady and Ball, 1984] Brady, R. M. and Ball, R. C. (1984). Fractal growth of copper electrodeposits. *Nature*, 309:225.

[Carleson and Makarov, 2001] Carleson, L. and Makarov, N. (2001). Aggregation in the plane and Loewner's equation. *Commun. Math. Phys*, 216:583 – 607.

[Carleson and Makarov, 2002] Carleson, L. and Makarov, N. (2002). Laplacian path models. *J. Anal. Math*, 87:103.

[Couder et al., 2005] Couder, Y., Maurer, J., González-Cinca, R., and Hernández-Machado, A. (2005). Side-branch growth in two-dimensional dendrites. I. Experiments. *Phys. Rev. E*, 71:031602.

[Davidovitch et al., 1999] Davidovitch, B., Hentschel, H. G. E., Olami, Z., Procaccia, I., Sander, L. M., and Somfai, E. (1999). Diffusion limited aggregation and iterated conformal maps. *Phys. Rev. E*, 59(2):1368–1378.

[do Carmo, 1976] do Carmo, M. P. (1976). *Differential geometry of curves and surfaces*. Prentice-Hall.

[Fogedby, 2007] Fogedby, H. C. (2007). Stochastic Loewner evolution. arXiv:0706.1177v1 [cond-mat.stat-mech].

[Gruzberg and Kadanoff, 2004] Gruzberg, I. A. and Kadanoff, L. P. (2004). The Loewner equation: Maps and shapes. *Journal of Statistical Physics*, 114.

[Gubiec and Szymczak, 2008] Gubiec, T. and Szymczak, P. (2008). Fingered growth in channel geometry: a Loewner-equation approach. *Phys Rev E*, 77.

[Halsey, 2000] Halsey, T. C. (2000). Diffusion-limited aggregation: A model for pattern formation. *Physics Today*, 53(11).

[Hastings and Levitov, 1998] Hastings, M. B. and Levitov, L. S. (1998). Laplacian growth as one-dimensional turbulence. *Physica D*, 116(1-2):244–252.

[Jensen et al., 2002] Jensen, M. H., Levermann, A., Mathiesen, J., and Procaccia, I. (2002). Multifractal structure of the harmonic measure of diffusion limited aggregates. *Phys. Rev. E*, 65:046109.

[Kuhn and Argoul, 1994] Kuhn, A. and Argoul, F. (1994). Spatiotemporal morphological transitions in thin-layer electrodeposition: The Hecker effect. *Phys. Rev. E*, 49(5):4298–4305.

[Langer, 1980] Langer, J. S. (1980). Instabilities and pattern formation in crystal growth. *Reviews of Modern Physics*, 52.

[Löwner, 1923] Löwner, K. (1923). Untersuchungen über schichtliche konforme Abbildungen des Einheitskreises. *I. Math. Ann.*, 89:103 – 121.

[Mandelbrot, 1982] Mandelbrot, B. B. (1982). *The fractal geometry of nature*. Macmillian.

[Matsushita et al., 2004] Matsushita, M., Hiramatsu, F., Kobayashi, N., Ozawa, T., Yamazaki, Y., and Matsuyam, T. (2004). Colony formation in bacteria: experiments and modeling. *Biofilms*, 1:305–317.

[Mullins and Sekerka, 1963] Mullins, W. W. and Sekerka, R. F. (1963). Morphological stability of a particle growing by diffusion or heat flow. *J. Appl. Phys.*, 34(2):323.

[Mullins and Sekerka, 1964] Mullins, W. W. and Sekerka, R. F. (1964). Stability of a planar interface during solidification of a dilute binary alloy. *J. Appl. Phys.*, 35(2):444.

[Nehari, 1982] Nehari, Z. (1982). *Conformal mapping*. Dover Pubns.

[Nermoen, 2009] Nermoen, A. (2009). Unpublished results.

[Rohde and Schramm, 2005] Rohde, S. and Schramm, O. (2005). Basic properties of SLE. *Annals Math.*, 161. arXiv:math.PR/0106036v4.

[Saffman and Taylor, 1958] Saffman, P. G. and Taylor, G. I. (1958). The penetration of a fluid into a porous medium or Hele-Shaw cell containing a more viscous fluid. *Proc. Roy. Soc. London*, A 245:312 – 329.

[Schramm, 2000] Schramm, O. (2000). Scaling limits of loop-erased random walks and uniform spanning trees. *Isr. J. Math.*, 118:221–228. arXiv:math.PR/9904022v2.

[Schramm, 2006] Schramm, O. (2006). Conformally invariant scaling limits (an overview and a collection of problems). arXiv:math/0602151.

[Selander, 1999] Selander, G. (1999). *Two deterministic growth models related to diffusion-limited aggregation*. PhD thesis, Royal institute of technology, Stockholm.

[Shraiman and Bensimon, 1984] Shraiman, B. and Bensimon, D. (1984). Singularities in nonlocal interface dynamics. *Phys. Rev. A*, 30(5).

[Stauffer, 1985] Stauffer, D. (1985). *Introduction to percolation theory*. Taylor and Francis, London and Philadelphia.

[Szymczak and Ladd, 2006] Szymczak, P. and Ladd, A. J. C. (2006). A network model of channel competition in fracture dissolution. *Geophys. Res. Lett.*, 33:L05401.

[Witten and Sander, 1981] Witten, T. A. and Sander, L. M. (1981). Diffusion-limited aggregation, a kinetic critical phenomenon. *Phys. Rev. Lett.*, 47.

[Witten and Sander, 1983] Witten, T. A. and Sander, L. M. (1983). Diffusion-limited aggregation. *Phys. Rev. B*, 27.

[Zik and Moses, 1999] Zik, O. and Moses, E. (1999). Fingering instability in combustion: An extended view. *Phys. Rev. E*, 60(1):518–531.